Two-Dimensional Platinum Diselenide: Synthesis, Emerging Applications, and Future Challenges

Youning Gong[1], Zhitao Lin[2], Yue-Xing Chen[1], Qasim Khan[3], Cong Wang[1], Bin Zhang[4], Guohui Nie[4], Ni Xie[4], Delong Li[1] ✉

Youning Gong, Zhitao Lin, and Yue-Xing Chen contributed equally to this work.

✉ Delong Li, ldlong19890809@163.com

[1] Institute of Microscale Optoelectronics, College of Physics and Optoelectronic Engineering, Shenzhen University, Shenzhen 518060, People's Republic of China

[2] Faculty of Information Technology, Macau University of Science and Technology, Macau 519020, People's Republic of China

[3] Department of Mechanical and Mechatronics Engineering, University of Waterloo, Waterloo, ON, Canada

[4] Otolaryngology Department and Biobank of the First Affiliated Hospital, Shenzhen Second People's Hospital, Health Science Center, Shenzhen University, Shenzhen 518060, People's Republic of China

HIGHLIGHTS

- A comprehensive review of the recent development of two-dimensional (2D) PtSe$_2$ synthesis strategies has been extensively surveyed.

- The applications of 2D PtSe$_2$ materials in areas, including opto/electric devices, photocatalysis, hydrogen evolution reaction, and sensors, have been reviewed.

- Current challenges in the development of 2D PtSe$_2$ materials are identified, and outlooks toward unexplored research areas are suggested.

ABSTRACT In recent years, emerging two-dimensional (2D) platinum diselenide (PtSe$_2$) has quickly attracted the attention of the research community due to its novel physical and chemical properties. For the past few years, increasing research achievements on 2D PtSe$_2$ have been reported toward the fundamental science and various potential applications of PtSe$_2$. In this review, the properties and structure characteristics of 2D PtSe$_2$ are discussed at first. Then, the recent advances in synthesis of PtSe$_2$ as well as their applications are reviewed. At last, potential perspectives in exploring the application of 2D PtSe$_2$ are reviewed.
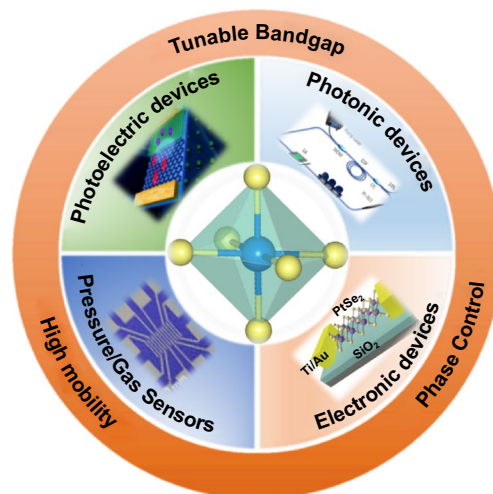
1 Introduction

Since graphene was discovered in 2004 [1], two-dimensional (2D) materials have attracted extensive attention due to their unique structure and outstanding properties [2–7]. Recently, layered 2D transition metal dichalcogenides (TMDCs) materials have become one of the hottest research topics due to a large potential in future nanoelectronics [8–15]. Unique physical phenomenon confining the transport of charge and heat in unique layered structure, which are not easily observed or measured in the related bulk crystal, has endowed them an attractive and promising 2D material for electronic, optoelectronic, and spintronic applications [16–19]. Different from the zero-band gap of graphene, TMDCs with tunable finite band gap and significant transitional behavior are more suitable for fabricating high-performance electronic and optoelectronic devices. In the last decades, group-6 TMDCs (such as MoS_2, $MoSe_2$, $MoTe_2$, WS_2, and WSe_2) which occur naturally in the 2H phase have attracted the most attention [18–22]. However, group-10 TMDCs (such as $PtSe_2$, PtS_2, $PdSe_2$, and PdS_2) which occur naturally in the 1T phase have been theoretically predicted as an outstanding material [23–30]. In addition, experimentally demonstrated distinct properties of group-10 TMDCs have made it prominent than other state-of-the-art 2D materials.

Among 2D group-10 noble TMDCs materials, platinum diselenide ($PtSe_2$) has emerged as promising materials for investigating quasiparticle interactions and for developing photoelectric devices [31–33]. Single-layer and few-layer $PtSe_2$ are p-type semiconductors, and thicker $PtSe_2$ exhibit typical semimetallic characteristics [27, 34]. Recently, due to their outstanding properties including widely tunable band gap, high carrier mobility, and excellent air stability, $PtSe_2$ has become increasingly fascinating in the 2D materials research [34–37]. 2D $PtSe_2$ has exhibited potential in many areas such as photocatalytic, hydrogen evolution reaction, electronic, and optoelectronic devices [38–40].

As an emerging 2D material, $PtSe_2$ possesses not only the merits of previously discussed 2D materials, but also many unique advantages. For examples, $PtSe_2$ exhibits a strong layer-dependent band structure. Bulk $PtSe_2$ exhibits semimetallic character, while monolayer and few-layer $PtSe_2$ are semiconductors [25, 41–43]. Moreover, $PtSe_2$ exhibits anisotropic carrier mobility along different directions. The theoretically calculated carrier mobility

of $PtSe_2$ is larger than 3250 cm^2 $V^{-1}S^{-1}$ (x direction) and 16,300 cm^2 $V^{-1}S^{-1}$ (y direction) at room temperature, respectively [28]. The theoretically predicted carrier mobility is at least 8 times larger than that of MoS_2 (about 410 cm^2 $V^{-1}S^{-1}$ for x direction and 430 cm^2 $V^{-1}S^{-1}$ for y direction) [28]. The outstanding inherent properties (including tunable band gap and carrier mobility) of $PtSe_2$ are comparable to black phosphorus (BP), but the stability of $PtSe_2$ is much better than BP [44–46]. Besides, experimental and theoretical studies have proven the intriguing transport properties and interesting spin physics of $PtSe_2$. Overall, these outstanding properties motivating further studies of the electrical transport properties, optoelectronic properties, and piezo-resistivity of 2D $PtSe_2$.

Herein, we divulge a comprehensive review based on experimental and theoretical research evolution on 2D layered $PtSe_2$, covering the progress, challenges, and prospects in future 2D material. The crystal structure, electronic band structure, and properties of few-layer $PtSe_2$ are introduced to give an overview of this material. Next, some recent progress on the various methods to synthesis monolayer and few-layer $PtSe_2$, including mechanical exfoliation, chemical vapor deposition (CVD), thermally assisted conversion (TAC), molecular beam epitaxy (MBE), and chemical vapor transport (CVT), are discussed in detail. Furthermore, the applications of 2D $PtSe_2$ in many areas, including photodetector, field effect transistors (FETs), mode-locked laser, photocatalytic, hydrogen evolution reaction (HER), and sensors, are highlighted. At last, the perspectives and outlooks for the 2D $PtSe_2$ materials are concluded.

2 Structure of 2D $PtSe_2$

2.1 Crystal Structure

Generally, there are two common structural phases for monolayer TMDCs, which are characterized by either octahedral trigonal prismatic (2H or D_{3h}) or (1T or D_{3d}). Unlike group-6 TMDCs, group-10 TMDCs tend to form $d2sp3$ hybridization due to group-10 metal atoms hold rich d-electrons and less d orbitals are involved. As a result, group-10 TMDCs lead to the generation of the thermodynamically favored 1T-phase. The 2D layered structure of TMDCs (such as PtS_2/$PtSe_2$/
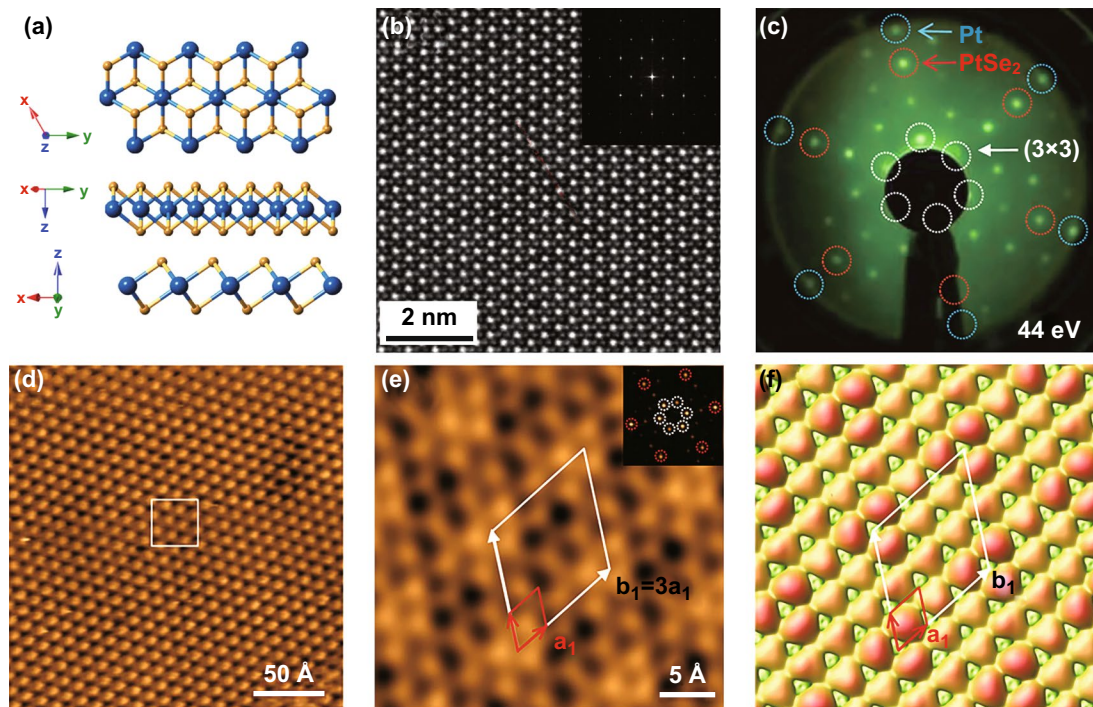
Fig. 1 Simulated and characterized crystal structure of PtSe₂. **a** Crystal structure of $PtSe_2$ from different view. The gold balls represent Se atoms and blue balls represent Pt atoms. Reproduced with permission [33]. Copyright 2019, Springer Nature. **b** HR-STEM image of a few-layer PtSe₂, inset: fast Fourier transform of the image. Reproduced with permission [28]. Copyright 2018, John Wiley and Sons. **c** LEED pattern of a monolayer PtSe₂ film on Pt substrate. **d** Large scale and **e** atomic resolution STM image of monolayer PtSe₂ film. **f** Simulated STM image of PtSe₂ by DFT calculation. Reproduced with permission [25]. Copyright 2015, American Chemical Society

$PtTe_2$ and $PdS_2/PdSe_2/PdTe_2$) has been proposed in 1950s since the pioneering work of Kjekus et al. and Grønvold et al. [47–49]. As a rising star of group-10 TMDCs, PtSe₂ has a thermodynamically favored 1T-phase structure and the atoms stack in the AA arrangement [28, 50].

PtSe₂ crystal belongs to the $D_{3d}^3(P3m1)$ space group of the trigonal system [34, 51, 52]. The crystal structure of PtSe₂ from different view is shown in Fig. 1a. Many techniques have been employed to characterize the atomic structure of monolayer PtSe₂, such as high-resolution scanning transmission electron microscope (HR-STEM), scanning tunneling microscope (STM), low energy electron diffraction (LEED), and density functional theory (DFT) calculation. As shown in Fig. 1b–f, the HR-STEM image, LEED patterns, STM images, and simulated STM images are presented, respectively. Figure 1b shows the representative HR-STEM image of PtSe₂. The fast Fourier transform of the image (inset of Fig. 1b) shows hexagonal structure and confirms the single-crystalline feature of the few-layer PtSe₂ samples. The HR-STEM image of PtSe₂ clearly shows that each Pt atom is in a tilted octahedral site

and surrounded by six Se atoms, which is consistent with the octahedral structure of 1T phase TMDCs [28, 53, 54].

As shown in Fig. 1c, hexagonal diffraction spots from monolayer PtSe₂ film are observed in a LEED pattern. The STM image and enlarged atomic resolution image of monolayer PtSe₂ are shown in Fig. 1d, e. By employing LEED, STEM, and STM methods, the atomic structure of PtSe₂ and lattice constant ($a_1 = 3.7$ Å, shown in Fig. 1e) are experimentally defined. Moreover, Wang et al. [25] conducted the DFT simulation based on the structure parameters obtained from the experimental characterizations. The simulated STM image is shown in Fig. 1f, and the results are well consistent with the STM observation results, which strongly demonstrated the highly crystalline structure of the 2D layered PtSe₂.

2.2 Electronic Band Structure

The electronic structure of 2D layered TMDCs materials strongly depends on the coordination environment of
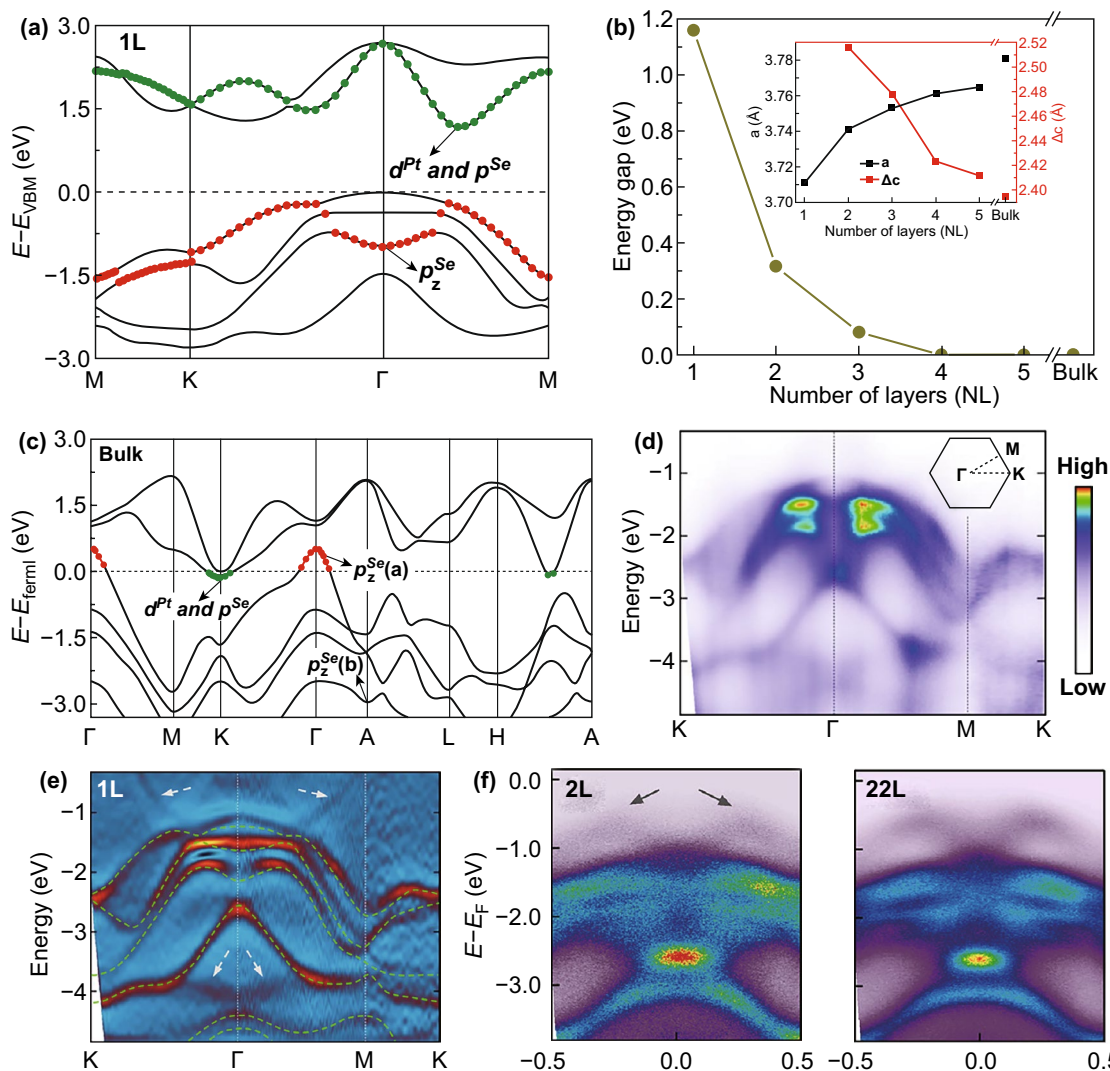
Fig. 2 Electronic structure of PtSe$_2$. **a** Band structure of monolayer PtSe$_2$. Reproduced with permission [28]. Copyright 2018, John Wiley and Sons. **b** Energy gap evolution as a function of number of layers (NL) for PtSe$_2$. Inset: layer dependence of lattice constant versus NL. Reproduced with permission [27]. Copyright 2019, Elsevier. **c** Band structure of bulk PtSe$_2$. Reproduced with permission [28]. Copyright 2018, John Wiley and Sons. **d** ARPES spectra and **e** corresponding second derivative spectra of monolayer PtSe$_2$. Reproduced with permission [25]. Copyright 2015, American Chemical Society. **f** ARPES spectra of bilayer and 22-L PtSe$_2$. Reproduced with permission [43]. Copyright 2015, American Chemical Society

transition metal and its d electron count [23]. PtSe$_2$ presents a layer-dependent band structure with dimensional reduction from bulk to monolayer. Zhao et al. [28] found that the monolayer PtSe$_2$ is an indirect semiconductor and the band gap of monolayer PtSe$_2$ is about 1.17 eV. Figure 2a shows the band structure of monolayer PtSe$_2$. The valence band maximum (VBM) of monolayer PtSe$_2$ situated at the Γ point, which comprised of the p_x and p_y orbitals of Se atoms ($p^{Se}_{x \text{ and } y}$). The conduction band minimum (CBM) of monolayer PtSe$_2$ is situated between the Γ and M points, which

is dominated by d states of Pt and p states of Se. The band gap of PtSe$_2$ abruptly decreased with the increased number of layers (NL), due to the exceptionally strong interlayer electronic hybridization of p_z orbital of Se atom (p^{Se}_z).

Figure 2b presents the band gap evolution of PtSe$_2$ as function of NL. The band gap of PtSe$_2$ shows a sharp decrease as the NL increased. As the NL larger than four the PtSe$_2$ shows a semiconductor-to-metallic transition. With increase in stacked layers, the energy level of VBM exceeds that of CBM between Γ and M because of the increase in

interlayer electronic hybridization [23, 28]. As a result, a semiconductor-to-semimetal evolution occurred. It has been proved that thicker $PtSe_2$ (layer numbers large than four or five) becomes semimetallic without a band gap [25, 28, 55]. As shown in Fig. 2c, the band gap structure of bulk $PtSe_2$ explicitly shows the semimetallic characteristics, and the CBM moves from a point between the Γ and M to the K point due to the strong interlayer interaction of $PtSe_2$ [28].

In 2015, Wang et al. [25] experimentally measured the band structure of monolayer $PtSe_2$ for the first time by using angle-resolved photoemission spectroscopy (ARPES). Figure 2d shows the ARPES spectra data measured along the high symmetry direction K–Γ–M–K in the hexagonal Brillouin zone at photon energy of 21.2 eV. As shown in Fig. 2e, the location of VBM and CBM in the derivative spectra indicates that monolayer $PtSe_2$ is a semiconductor. The ARPES results show excellent quantitative agreement with the DFT simulation results. With this pioneer work, ARPES has become one of the most important techniques to investigate the electronic structure of $PtSe_2$ [43, 56, 57]. In order to study the layer-dependent electronic structure, Yan et al. measured ARPES data along the Γ−K direction [43]. As indicated by gray arrow in Fig. 2f, an M shape band was observed in thicker $PtSe_2$ (NL ≥ 2). Moreover, the M-shaped band moves toward the Fermi energy as the atomic layers increased, indicating a reduction of the band gap. Therefore, the ARPES results provide direct evidences for the layer-dependent band gap of $PtSe_2$ as theoretically predicated [27, 58, 59].

3 Properties of 2D PtSe₂

This section highlights the unique properties of 2D $PtSe_2$ such as band gap tenability, phase transition, and vibration spectroscopic and optical properties. The band gap tuned by various kinds of external parameters has been introduced at first. Then, the phase transition of 1T phase, 1H phase, and non-layered $PtSe_2$ are reviewed. At last, the vibration spectroscopic and optical properties are introduced in details.

3.1 Band Gap Tunability

It has been widely proved that the band structure of 2D TMDCs can be tuned by doping, defect engineering,

strain, and external electric field [60–64]. Besides the inherent thickness-dependent band gap, band gap of $PtSe_2$ also can be tuned by applying external parameters. For example, band gap of few-layer $PtSe_2$ can be tuned over a wide range by applying strain. The band structure of monolayer $PtSe_2$ with symmetrical biaxial compressive strains and symmetrical tensile strains reveals the band structure evolution, as shown in Fig. 3a, b [65]. Du et al. [66] have also demonstrated that the band gap decreases approximately linearly with the increased tensile strain, but it is different for the band gaps evolution under compressive strain. As shown in Fig. 3a, monolayer $PtSe_2$ exhibits a direct gap semiconductor characteristic as the compressive strain reaches − 8%. The same transformation has also been reported by other published papers [52, 66–68]. Moreover, due to the chemical interaction (*p* orbital coupling) between Se atoms of the two layers, a reversible semiconducting metallic transition bilayer $PtSe_2$ under critical vertical strain, as shown in Fig. 3c [52]. Besides strain engineering, doping also has significant effect on the band structure of 2D $PtSe_2$ [36, 39, 69]. As shown in Fig. 3d, the band structures of the halogen elements (including F, Cl, Br, and I)-doped monolayer $PtSe_2$ have been calculated by DFT [36]. As compared with pristine monolayer $PtSe_2$, the localized impurity states located close to the CBM are identified. The band structure of transition metal-doped $PtSe_2$ has been simulated by Kar et al. by using DFT [69]. And they found that group IIIB, VB, VIII8, VIII9, and IB transition metal-doped monolayer $PtSe_2$ exhibits half-metallic properties together with spin gap. Besides, the other transition metal-doped $PtSe_2$ exhibits tunable semiconducting or tunable magnetic semiconducting properties.

3.2 Phase Transition

Due to the strong covalent bond strength and weak interlayer interaction, the structure of 2D materials strongly depends on varying external effects (pressure, strain, irradiation, annealing, or lithiation) [23]. Phase transition can be induced by ionic intercalation, high pressure, strain, thermal treatment, and external electrical and magnetic field. Since 1T-$PtSe_2$ is a very stable structure, it is difficult to expect a continuous phase transition unless inducing additional electron beam irradiation and annealing treatment.
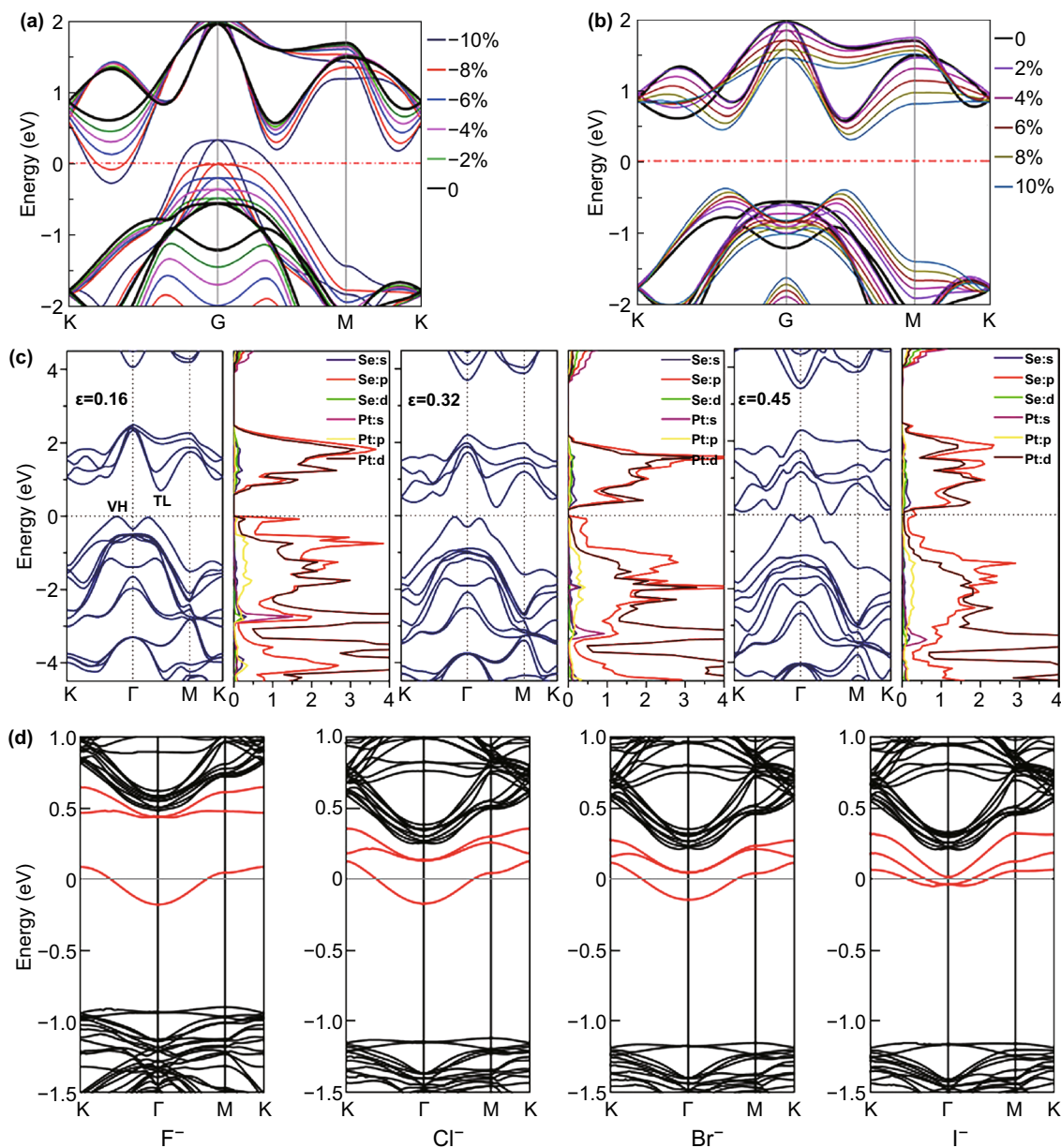
Fig. 3 Band structure engineering of PtSe$_2$. Computed band structure of the monolayer PtSe$_2$ with symmetrical biaxial compressive (**a**) and tensile strains (**b**). Reproduced with permission [65]. Copyright 2018, American Chemical Society. **c** Band structure and density of state of bilayer PtSe$_2$ under vertical compressive strain (ε = 0.16, 0.32, and 0.45). Reproduced with permission [52]. Copyright 2016, American Chemical Society. **d** Computed band structure of the F-doped, Cl-doped, Br-doped, and I-doped monolayer PtSe$_2$. Reproduced with permission [36]. Copyright 2018, American Physical Society

As show in Fig. 4a, b, Lin et al. studied the reversible phase transition of 1T phase and 1T/1H patterned PtSe$_2$ by using in situ STM [70]. The homogeneous 1T-PtSe$_2$ shown in Fig. 4a was directly synthesized on a Pt (111) substrate via a TAC process at 270 °C. As the 1T-PtSe$_2$ film annealed at 400 °C, periodic triangular pattern structure of alternating

1H/1T patterned phases formed. The STM images of the 1H/1T patterned phases are shown in Fig. 4b. Moreover, the triangular 1H/1T pattern reverts to a homogeneous 1T phase PtSe$_2$ by annealing the periodic triangular 1H/1T patterned PtSe$_2$ at 270 °C in Se steam atmosphere. However, Lin et al. found that the 1H/1T triangular pattern can be directly
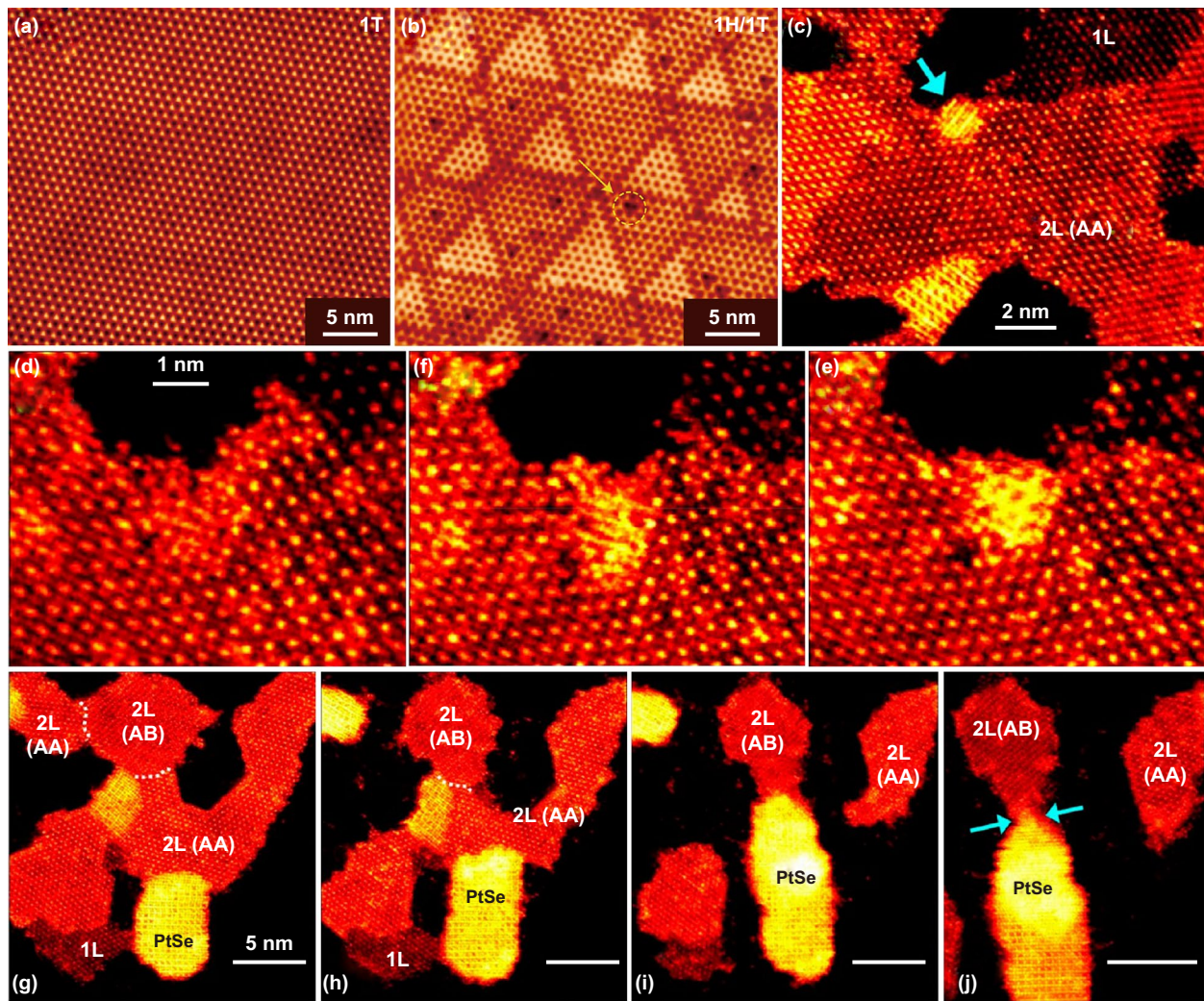
Fig. 4 In situ characterization of phase transitions of PtSe₂. STM images of **a** 1T-PtSe₂ and **b** 1H/1T patterned PtSe₂. Reproduced with permission [70]. Copyright 2017, Springer Nature. **c** PtSe₂ at the edge of bilayer PtSe₂. **d, e** Successive annular dark field STEM images at a position indicated by a cyan arrow in (**c**). **f** Time between images ~60 s. **g–j** Successive annular dark field STEM images at the position indicated by cyan arrows in (**j**). White dashed line indicated the grain boundary. **c–j** Reproduced with permission [75]. Copyright 2019, American Chemical Society

prepared by controlling the initial density of Se atoms during the TAC process. The DFT and experiment measurement show that the Se vacancies mediate the formation of 1H domains. This transformation process has been reported in other 2D materials, such as monolayer MoS_2 [71, 72] and $PdSe_2$ [73, 74].

In addition, Ryu et al. [75] demonstrated that 1T phase PtSe₂ can transform into non-layered 2D PtSe₂ ultrathin film. The phase transformation from 1T PtSe₂ into non-layered PtSe₂ crystals induced due to the Se loss during the additional heating process at high temperature (550 °C). As shown in Fig. 4c, d, the rearrangement and restacking of the

atoms have been in situ observed by taken successive annular dark field scanning transmission electron microscope (ADF-STEM) images. It can be found that the phase transition occurred only in the bilayer region. Further characterization of the phase transition process has been observed by constructed AA stacking and AB stacking bilayer PtSe₂. As shown in Fig. 4e–g, the phase transition occurs only in the AA stacking PtSe₂ region. As the PtSe₂ film was heated, the non-layered PtSe₂ structure continued to expand and blocked at the grain boundary.

Besides the annealing and heating process, plasma treatment process has also been proved as an efficient method
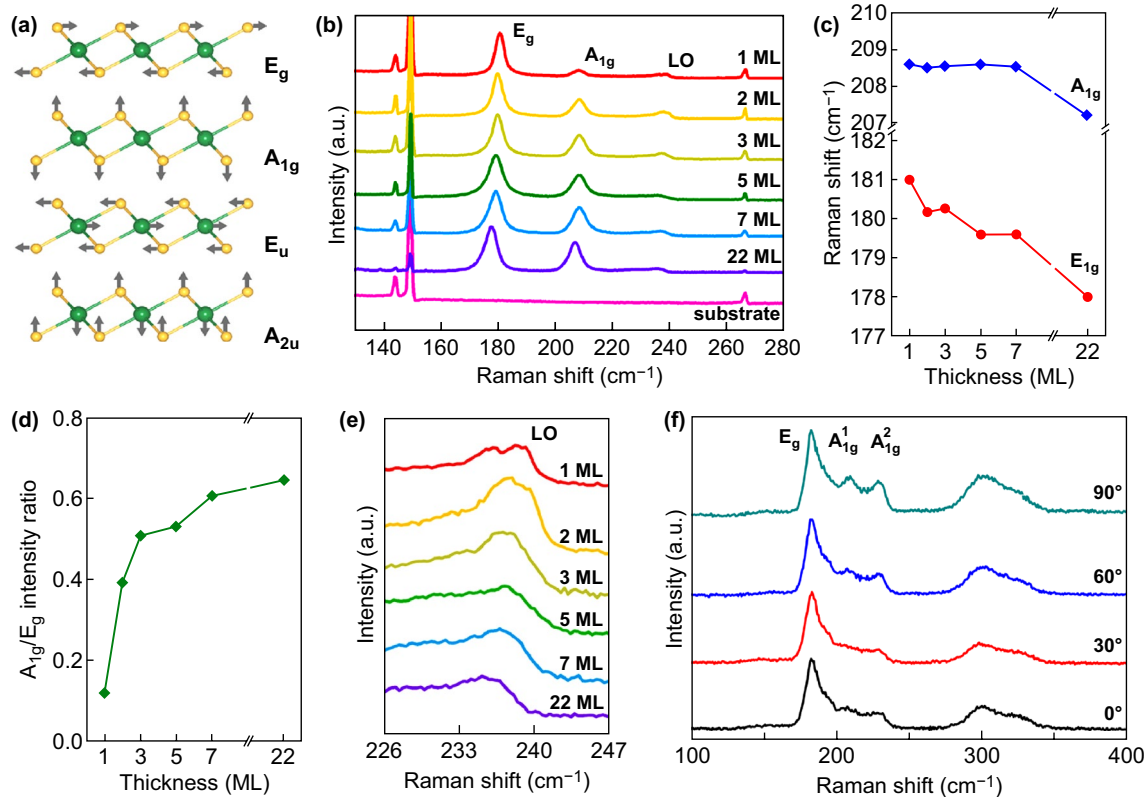
Fig. 5 Vibrational properties of PtSe$_2$. **a** Schematic views of Raman vibrational modes in PtSe$_2$. **b** Thickness-dependent Raman spectra of PtSe$_2$. **c** The E_g and A_{1g} peak positions of PtSe$_2$ with increase in thickness. **d** Analysis of thickness dependent of A_{1g}/E_g intensity ratio. **a–d** Reproduced with permission [43]. Copyright 2017, IOP Publishing. **e** Zoom in Raman spectra of the LO mode. **f** Polarization-dependent Raman spectra of PtSe$_2$. Reproduced with permission [28]. Copyright 2018, John Wiley and Sons

to induced phase transition in 2D PtSe$_2$. Yang et al. [76] reported an inductively coupled plasma treatment method to selectively controlling the thickness of PtSe$_2$ flakes. With the decrease in thickness, PtSe$_2$ flake transforms from a semimetal to semiconductor. This is well consistence with the prediction concerning their intrinsic thickness-dependent band structure. However, Shawkat et al. discovered a reversed transition of semiconducting to metallic as the PtSe$_2$ film irradiated by plasma. Shawkat et al. [77] realized a semiconductor-to-metallic transition in wafer-scale PtSe$_2$ film by controlled plasma irradiation. Extensive structural and chemical characterization has proven that large concentration of near atomic defects and selenium vacancies introduced by the plasma irradiations induced the transition of semiconductor to metallic.

The phase transition driven by thermal heating makes it possible for fabricating lateral heterojunctions composed of 1T-PtSe$_2$, 1H-PtSe$_2$, and PtSe. The electronic properties of 2D PtSe$_2$ materials can be modulated by the induced phase

transition, which offers new opportunities in both fundamental research and (opto-) electronic devices applications.

3.3 Vibration Spectroscopic Modes

Raman spectroscopy is a powerful and nondestructive optical characterization technique to study the lattice vibrations as well as electron–phonon coupling of 2D materials. Due to the strong interlayer coupling and hybridization, the Raman spectra of PtSe$_2$ exhibit interesting anomalous changes.

The schematic diagram of four Raman active vibrational modes in PtSe$_2$ is shown in Fig. 5a [43]. The A_{1g} mode and E_g mode are originated from the out-of-plane vibration and the in-plane vibration of Se atoms, respectively. Figure 5b exhibits the Raman spectra of PtSe$_2$ with different thickness. As shown in Fig. 5b, the Raman spectra of 2D PtSe$_2$ with different thickness, laser wavelength, and laser polarization were systematically studied. Three primary Raman peaks

which allocated to E_g (~ 180 cm^{-1}), A_{1g} (208.5 cm^{-1}), and LO (~ 240 cm^{-1}) modes are observed. As the Raman spectra are normalized to the E_g peak, the relative intensity of the A_{1g} peak exhibits an obvious decreasing as the thickness decreased. As shown in Fig. 5c, the peak positions of the E_g and A_{1g} mode are extracted and plotted as a function of number of layers. The position of E_g mode exhibits a clear red shift with increase in thickness. However, the position of A_{1g} mode is almost unchanged for few-layer PtSe$_2$ and exhibits an obvious red shift as the number of layers larger than 22 layers. The layer dependence of Raman spectra properties may be attributed to the strong long-range interlayer interactions [78, 79]. To further study the relationship between the thickness and Raman spectra, the intensity ratio of the A_{1g} peak to E_g peak is extracted and plotted in Fig. 5d. The extracted thickness\intensity ratio is well consistent with the enhanced van der Waals interactions between the layers in thicker 2D materials [68, 78, 80]. Besides the distinct E_g and A_{1g} modes, Raman peaks ascribed to less prominent LO

mode, which attributed to a combination of the in-plane E_u and out-of-plane A_{2u} vibrations, are also observed [43, 55]. The enlarge spectra in Fig. 5e show the thickness-dependent position of the LO peaks. With increase in number of layers, the LO peaks change into a broader hump and the intensity decreased.

Moreover, the vibration modes of PtSe$_2$ were further characterized by polarization-dependent Raman spectra [28, 78]. As shown in Fig. 5f, the variation of the polarization of the incident light has no effects on the intensity of E_g peak (around 180 cm^{-1}), which confirming the in-plane nature of this mode. However, an obvious intensity decrease in the A_{1g} peak (around 208 cm^{-1}) and LO peak (around 240 cm^{-1}) depending on light polarization is observed. The decrease in the intensity of A_{1g} peak and LO peak confirms the out-of-plane vibration nature of these two modes. It has been proved that these Raman peaks have been observed in the mechanic exfoliated PtSe$_2$ single crystal as well as the PtSe$_2$ film grown via TAC process [28, 78].
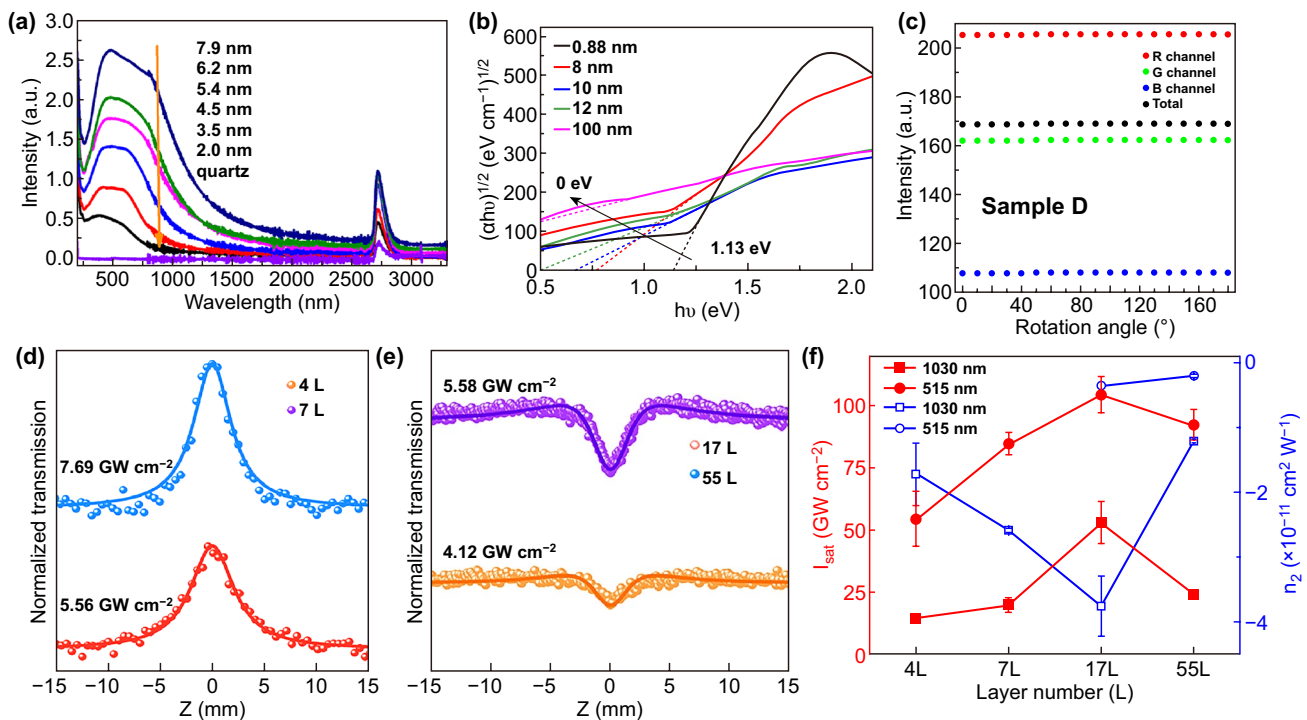

Fig. 6 Optical properties of PtSe$_2$. **a** Thickness-dependent UV–Vis–IR absorption spectra of PtSe$_2$ film on sapphire substrate. Reproduced with permission [82]. Copyright 2019, AIP Publishing. **b** Thickness-dependent Tauc plots of PtSe$_2$ film. Reproduced with permission [28]. Copyright 2018, John Wiley and Sons. **c** Intensity of red channel, green channel, blue channel, and the total intensity at different rotation angle. Reproduced with permission [81]. Copyright 2019, IOP Publishing. **d**, **e** Open aperture Z-scan results of 4L, 7L, 17L, and 55L PtSe$_2$ films at 1030 femtosecond pulse excitation. **f** Saturation irradiance (IS_{at}) and **g** nonlinear refractive index (n_2) of 4L, 7L, 17L, and 55 L PtSe$_2$ films at 1030 nm and 515 nm. Reproduced with permission [84]. Copyright 2019, John Wiley and Sons

3.4 Optical Properties

3.4.1 Layer-Dependent Optical Absorption Spectra

The refractive index and extinction coefficient are fundamental properties of a material that not only determines its optical responses, but also directly connects to its complex permittivity and dielectric constant. Wang et al. measured the refractive index and extinction coefficient of the $PtSe_2$ (~3 nm) in the wavelength range from 200 to 900 nm by using spectroscopic ellipsometry [31]. The refractive index of the ultrathin $PtSe_2$ film increased from 1.5 to 4.5 as the wavelength increased from 200 to 900 nm. However, the extinction coefficient of the ultrathin $PtSe_2$ film is almost unchanged and maintained around 2.4. Xie et al. [81] also measured the refractive index and extinction coefficient of the $PtSe_2$ film in the wavelength range from 360 to 1700 nm. The refractive index and extinction coefficient values are strongly dependent on the thickness of $PtSe_2$ film. By analyzing the spectroscopic ellipsometry results, the values of refractive index and extinction coefficient increased as the film thickness increasing.

As shown in Fig. 6, the thickness-dependent optical absorption spectra of $PtSe_2$ films were measured in the wavelength range of 200–3300 nm [82]. As shown in Fig. 6a, $PtSe_2$ exhibits a broadband absorption response with a smooth absorption band in the wavelength range of 400–800 nm. However, in the wavelength range of 800–2200 nm, the absorption intensity decreased as the wavelength increased. In the range of 2200–3300 nm, $PtSe_2$ still exhibits a broadband absorption and the intensity almost unchanged in this wavelength range. Besides, the absorption spectra of thicker $PtSe_2$ film exhibit an obvious red shift. Usually, semiconductors cannot absorb light with energy much smaller than the band gap, but $PtSe_2$ film exhibits strong light absorption in a broadband wavelength range from deep ultraviolet to mid-infrared (mid-IR) [28, 66, 81–83]. The strong IR light absorption of $PtSe_2$ mainly attributes to the semimetallic components of the films [81, 82].

The band gap of semiconductors can be easily experimentally measured by using optical absorption spectra. The layer-dependent Tauc plots of $PtSe_2$ are presented in Fig. 6b. With increase in thickness, the absorption edge of Tauc plot shows an obvious red shift. The band gaps of monolayer $PtSe_2$ are well consistence with the DFT calculation results. Meanwhile, the transition from semiconductor to semimetal of $PtSe_2$ has been verified by the layer-dependent Tauc plots, which is also well agreement with DFT calculation.

3.4.2 Isotropic Optical Properties

Xie et al. [81] studied the optical isotropy properties by using polarized optical imaging method and polarization-dependent optical absorption measurement, and they ascertained the optical isotropy in the 2D $PtSe_2$. As shown in Fig. 6c, the intensity of the red, green, blue (RGB) channels and the total intensity at different rotation angles were extracted from the polarized optical images of a $PtSe_2$ film (~5.3 nm). As the rotation angle changed, the intensity of RGB channels and total intensity are almost unchanged, which indicate the optical isotropy of $PtSe_2$. The absorption spectra in the range of 400–800 nm under polarization directions of 0° (horizontally), 90° (vertically), and non-polarized light for $PtSe_2$ film (~5.3 nm) were measured. These absorption spectra are well consistent with each other, indicating the in-plane isotropic optical absorption in $PtSe_2$ film.

3.4.3 Nonlinear Optical Properties

Nonlinear optical (NLO) properties of 2D materials have been taken as the forefront of the research, which are crucial for developing high-performance ultrafast laser and optoelectronic devices [85–93]. $PtSe_2$ has nonlinear effects in a wide wavelength range due to its narrow band gap. Tao et al. [94] investigated the NLO properties of TAC-synthesized $PtSe_2$ films. A modulation depth of 12.6% and saturation fluence of 17.1 $\mu J\ cm^{-2}$ were obtained based on the NLO transmittance curve. The saturable absorption (SA) characteristics of the transverse-electric and transverse-magnetic modes of $PtSe_2$ are studied by Zhang et al. [95] Modulation depth of 4.90% (transverse-electric modes) and 1.11% (transverse-magnetic modes) are obtained based on the NLO transmittance curves.

The NLO properties of few-layer $PtSe_2$ have been systematic studied by using the Z-scan method and pump–probe–technique [84]. As shown in Fig. 6d, two small peaks near the symmetrical valley are observed in the open aperture (OA) signals of 4L and 7L $PtSe_2$ films, which suggest the OA signals

consist of both SA and two-photon absorption (2PA) response at 1030 nm. However, there are no peaks observed near the symmetrical valley in the OA signals of 17L and 55L PtSe$_2$ (Fig. 6e), which indicate the pure SA response. The evolution of the saturation (IS$_{at}$) and irradiance nonlinear refractive index (n_2) are extracted and plotted in Fig. 6f, g. The large IS$_{at}$ at 515 nm indicates that PtSe$_2$-based saturable absorber possesses higher saturation intensity in visible range than that in near-IR range. Besides, the large value n_2 of PtSe$_2$ suggests the huge potential to developing self-defocusing materials in NLO devices.

4 Synthesis Methods

Generally, the crystal structure, crystallinity, and properties of 2D PtSe$_2$ are strongly related to the synthesis process. It is still challenging to prepare 2D PtSe$_2$ with the desirable thickness, lateral size, and microstructure for specific applications. Indeed, various strategies have been proposed to prepare 2D PtSe$_2$, specially aiming to materials with high quality and large lateral size. Up to now, great achievements have been made to prepare 2D PtSe$_2$ with controllable thickness, morphology, and lateral size. In this section, different synthesis methods
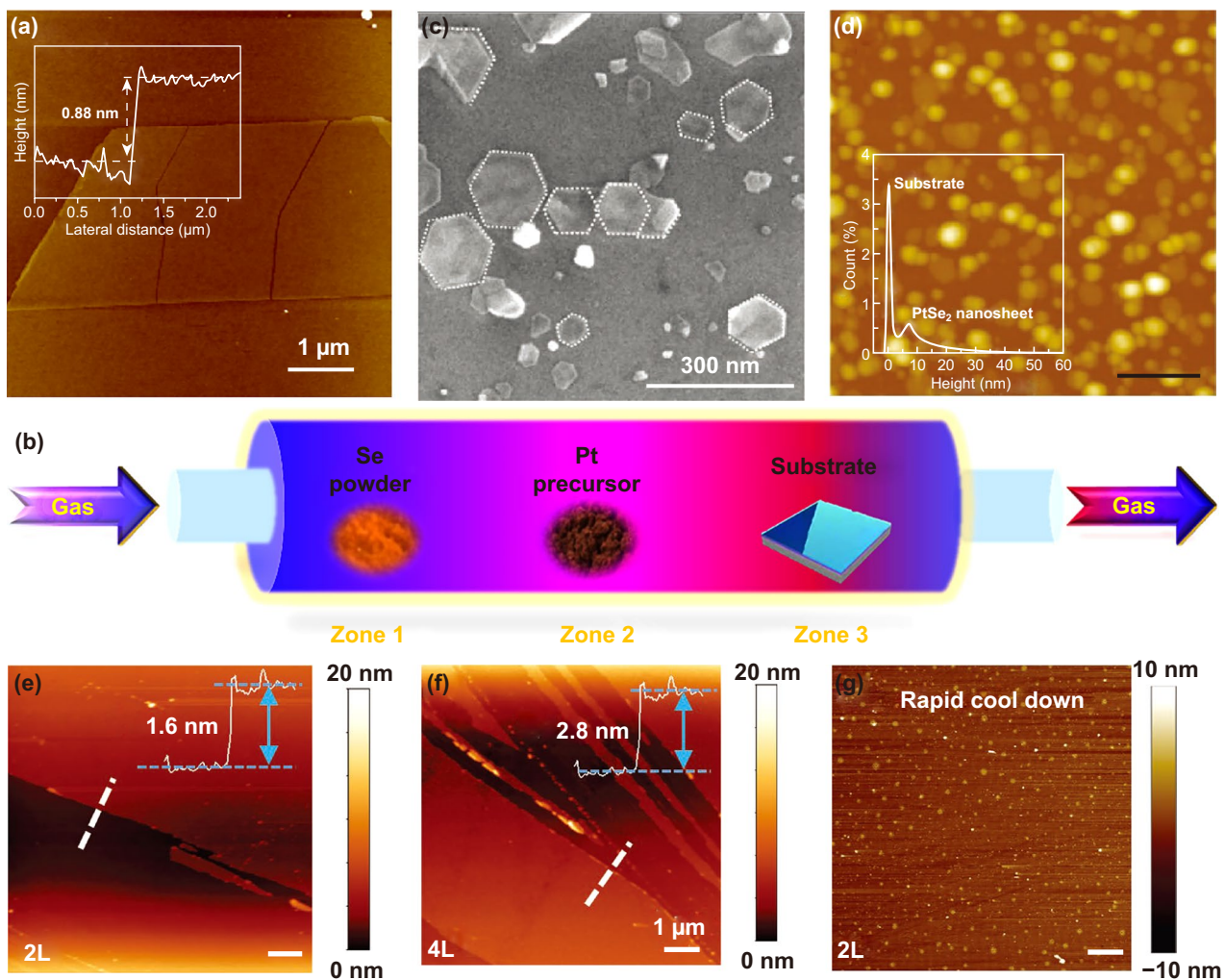

Fig. 7 2D PtSe$_2$ prepared by Mechanical exfoliation/CVD. **a** AFM image of the exfoliated monolayer PtSe$_2$ and corresponding height profiles. Reproduced with permission [28]. Copyright 2018, John Wiley and Sons. **b** Schematic diagram of the three zones CVD system for the synthesis of 2D PtSe$_2$. **c** SEM morphology of the PtSe$_2$ nanosheets synthesized by CVD process. **d** AFM image of the PtSe$_2$ nanosheets synthesized by CVD process. **c**, **d** Reproduced with permission [106]. Copyright 2016, John Wiley and Sons. The AFM image of the **e** bilayer and **f** four layer PtSe$_2$ film and corresponding height profiles [107]. **g** AFM image of the bilayer PtSe$_2$ synthesized via rapid cool down process. **e–g** Reproduced with permission [107]. Copyright 2019, John Wiley and Sons

for preparing 2D $PtSe_2$ are systematically discussed. CVD and TAC are the most widely studied methods to synthesis 2D $PtSe_2$. Moreover, the other methods such as mechanical exfoliation and CVT have also been studied.

4.1 Mechanical Exfoliation

Mechanical exfoliation (ME) is one of the most commonly used methods to prepare high quality 2D materials [96–99]. Monolayer or few-layer 2D materials obtained by this method can maintain their intrinsic structure and are suitable for fundamental research. Mechanical exfoliation has been extensively exploited to prepare monolayer or few-layer 2D materials, such as graphene, BP, nitride, TMDCs, and MXene. The mechanical exfoliation process is a relatively simple and fast process by repeating adhesion and splitting. As the monolayer or few-layer 2D materials attached on the surface of scotch tape, the as-prepared 2D materials can be easily transferred to selected substrate [1, 99]. In 2017, Zhao et al. [28] prepared monolayer $PtSe_2$ by using mechanical exfoliation. The high quality $PtSe_2$ bulk crystal was grown by CVT method. Ultrathin $PtSe_2$ was peeled from bulk $PtSe_2$ using a scotch tape, as shown in Fig. 7a. Huang et al. [100] prepared $PtSe_2$ nanoflakes with the thickness of ~ 70 nm by mechanical exfoliation its single crystal. However, mechanical exfoliated 2D materials can only fulfill the using demands of fundamental studies due to the limited yield and relatively small lateral size.

4.2 Chemical Vapor Deposition

CVD is an important synthesis method to prepare high quality 2D materials with scalable size, controllable thickness, and perfect crystal structure for both fundamental research and practical applications [101–104]. To date, various materials with controllable layer number, lateral size, and microstructure have been successfully prepared via CVD methods, such as graphene, TMDC, Xene, boron nitride, and MXene. Recently, the CVD growth of monolayer or few-layer 2D $PtSe_2$ has also attracted extensively attention and has been taken as a promising method to realize the large-scale growth of 2D $PtSe_2$.

$PtSe_2$ with controlled morphology can be synthesized by CVD process via precise tuning of the growth temperature, pressure, and precursors [83, 105–108]. Figure 7b

shows the typical schematic illustration of a 3-zone CVD growth setup, wherein the precursors are placed in different zone of the quartz tube. Typically, Se powder and $PtCl_4$ or H_2PtCl_6 powder are chosen as the precursors; the obtained $PtSe_2$ is found to be nearly hexagonal with the thickness ranging from 3.5 to 10 nm [106]. However, by tuning the growth temperature of zone 3 from 900 to 500 °C, Xu et al. successfully prepared polycrystalline $PtSe_2$ film with controlled thickness by tuning the growth time [107]. The morphology of the single-crystalline and polycrystalline $PtSe_2$ is shown in Fig. 7c–g, respectively. As shown in Fig. 7e–g, large area continuous $PtSe_2$ films with controlled thickness have been successfully synthesized via a one-step CVD process. Furthermore, the cooling down rate also has great effect to the surface morphology. The rapid cooling rate may suppress the diffusion of reactive atoms, leading to the formation of the multilayer island on the surface [107]. The multilayer islands on the surface of $PtSe_2$ thin film are shown in Fig. 7g.

The morphology, thickness, microstructure, and lateral size of 2D materials can be well controlled by precise controlling CVD growth parameters. The quality of the as-grown $PtSe_2$ can be determined by many factors including but not limited to the precursors, pressure, temperature, heating rate, and substrate. Thus, in-depth understanding of the CVD growth mechanism is beneficial to the improvement of scalability and controllability for $PtSe_2$ synthesis.

4.3 Thermally Assisted Conversion

TAC of pre-deposited metal on substrate is also an effective strategy to grow wafer-scale 2D materials [109–111]. $PtSe_2$ prepared by this method is a just simple chemical reaction, $Pt + 2Se = PtSe_2$. Direct selenization of the Pt film provides a simple and fast approach to obtain wafer-scale 2D $PtSe_2$ film.

The TAC process is a straightforward and simple route for synthesizing large-scale $PtSe_2$ with controlled thickness. Pt film with different thickness is initially deposited on a given substrate via a magnetron sputtering process or electron beam evaporate process. Then, the $PtSe_2$ film is prepared via the directly selenization process. As shown in Fig. 8a, the Se powder is placed at the upstream side in the tube furnace, and the Pt coated substrates are placed in the heating zone. During the selenization process, the growth
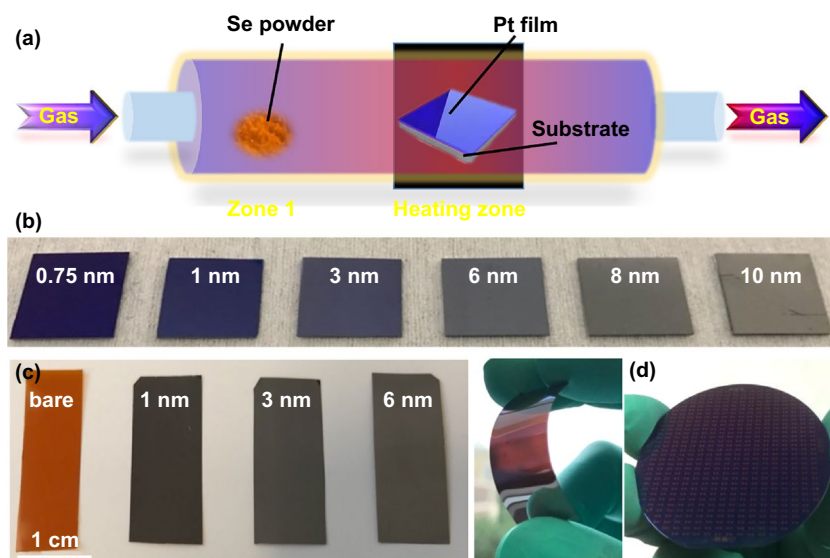
Fig. 8 Large-scale PtSe$_2$ film growth by TAC. **a** Schematic diagram of the CVD system for the synthesis of 2D PtSe$_2$ film by using TAC process. **b** Photograph of 2D PtSe$_2$ film on SiO$_2$/Si substrate with controlled thickness. **c** Photograph of 2D PtSe$_2$ film on polyimide substrate with controlled thickness. Reproduced with permission [114]. Copyright 2019, American Chemical Society. **d** Photograph of a wafer-scale PtS$_2$/PtSe$_2$ film on a 2-in. SiO$_2$/Si substrate. Reproduced with permission [117]. Copyright 2018, American Chemical Society

temperature is usually set to about 270-500 °C, while the pressure remains at about 80 mTorr with argon gas protection [25, 112, 113]. In 2015, Wang et al. [25] firstly fabricated a single crystal monolayer PtSe$_2$ by direct selenization of Pt (111). Han et al. [114] prepared large-scale 2D PtSe$_2$ with different thickness on SiO$_2$/Si substrate. Figure 8b shows the photograph of the PtSe$_2$ film with different thickness on SiO$_2$/Si substrate. The lateral size and thickness of PtSe$_2$ film can be controlled by modulating thickness of the pre-deposited Pt film [84, 115].

Since the pre-deposition process and post-selenization process are carried out in relatively mild condition, the PtSe$_2$ film can be prepared on arbitrary substrates. Besides the conventional Si [33, 115, 116], Si/SiO$_2$ [32, 33, 55, 94, 112, 114, 117–124], and Sapphire substrate [81, 125, 126], 2D PtSe$_2$ film has been successfully grown on fused quartz [31, 84, 125], fluorine-doped tin oxide (FTO) [127, 128], gallium nitride (GaN) [129], and polyimide [114]. Figure 8c shows the PtSe$_2$ on the surface of flexible polyimide [41, 114]. As shown in Fig. 8d, Yuan et al. [117] fabricated a wafer-scale PtSe$_2$/PtS$_2$ heterojunction film via two step TAC process on a SiO$_2$/Si wafer with 300-nm-thick Si dioxide. TAC process enables the growth of PtSe$_2$ on wafer-scale substrate, offering the throughput that can meet the demand for practical application.

4.4 Other Methods (Molecular Beam Epitaxial, CVT)

In addition to the aforementioned methods, some other approaches also have been reported to synthesize 2D PtSe$_2$. For example, some pioneer works have been reported that PtSe$_2$ can be prepared via a Sol–Gel solution process [130–134]. Umar et al. [135] reported the successful synthesis of scalable 2D PtSe$_2$ nanosheets via an aqueous-phase synthetic strategy for the first time. PtSe complexes precursors are initially prepared via surfactant-template self-assembly process. Then, the mesoporous 2D PtSe$_2$ nanosheets are prepared by thermal annealing the PtSe complexes precursors. As shown in Fig. 9a, the 2D PtSe$_2$ nanosheets with a thickness about 11–25 nm are synthesized, indicating that scalable PtSe$_2$ can be produced by a straightforward process to scalable produce PtSe$_2$. Pawar et al. [136] also prepared 2D PtSe$_2$ nanosheets by using the almost same method that Umar reported.

As a widely studied traditional crystal growth method, CVT has also been employed to direct synthesize 2D semiconductor materials, such as TiSe$_2$, MoS$_2$, WS$_2$, and ReS$_2$ [137–141]. Benefitting from the good controllability of the growth parameters, the properties, structure, and composition of 2D materials can be well regulated. In 2016, Yu et al. [33] successfully synthesized single crystal of PtSe$_2$
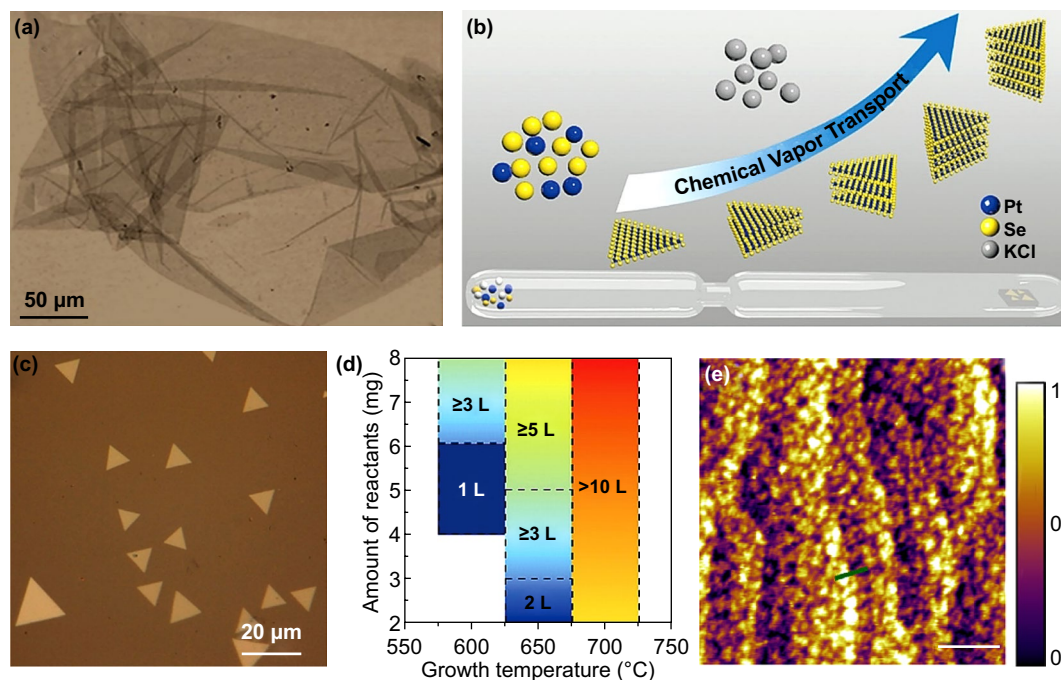
Fig. 9 2D PtSe$_2$ prepared by solution process/CVT/MBE. **a** Optical image of the PtSe$_2$ nanosheets prepared via an aqueous-phase reaction process. Reproduced with permission [135]. Copyright 2017, American Chemical Society. **b** Schematic diagram of the controlled synthesis of PtSe$_2$ by CVT. **c** Optical image of PtSe$_2$ triangle nanoflakes prepared by CVT. **d** Relationship of the layer numbers of the as-grown PtSe$_2$ triangle nanoflakes as a function of growth temperature and amount of reactants. Reproduced with permission [142]. Copyright 2019, John Wiley and Sons. **e** AFM image of the PtSe$_2$ grown on the bilayer graphene by MBE method. Reproduced with permission [43]. Copyright 2017, IOP Publishing

by using CVT method. This achievement makes it possible for us to grown 2D PtSe$_2$ by precise controlling the growth condition. Hu et al. [142] successfully synthesizes 2D PtSe$_2$ nanosheets with controlled thickness by using CVT. As shown in Fig. 9b, the schematic diagram of the CVT process is presented. The raw materials are put in a sealed the quart tube, while the substrate is placed in the other side of the quart tube. By carefully adjusting the amount of precursors and transport agent, triangular-shaped single-crystalline PtSe$_2$ flakes were obtained on the mica substrate. The optical morphology of the triangular-shaped single-crystalline PtSe$_2$ flakes is shown in Fig. 9c, and the relationship of the thickness with temperature and reactants is exhibited in Fig. 9d. However, only few papers have reported the synthesis of 2D

Table 1 Comparison of different synthesis methods to prepare 2D PtSe$_2$

Methods	Lateral size	Number of layers	Achievements	Challenges
ME	~Micrometers	Any number of layer	High quality	Uncontrollable
CVD	~Micrometers	1L~few layer	Single crystal high quality	Limited area
TAC	Wafer scale	Few layer to tens of nanometers	Continuous film of wafer-scale size	Polycrystalline film
				Surface roughness
CVT	~Centimeter	Nanoflakes to bulk	Large crystal	Long growth time
			High quality	Difficult to growth few-layer samples
MBE	~Centimeter	Few layer	Large scale	Complex
			High quality	Expensive
			Controlled thickness	Limited substrate

$PtSe_2$ by using CVT due to the complex growth condition. Since growth of bulk semiconductor crystal by CVT is much easier than direct growth 2D semiconductor materials, CVT is generally employed to grow high quality single-crystalline bulk materials, ultrathin 2D flakes are then peeled from bulk crystal by mechanical exfoliation [142–144]. For example, Zhao et al. [28] grow $PtSe_2$ single crystal by using CVT method and the air stable 2D $PtSe_2$ are peeled from the bulk $PtSe_2$ crystal.

Molecular beam epitaxy (MBE) has been playing an important role in the growth of high quality 2D materials film with controlled thickness [145, 146]. Yan et al. [43] successfully prepared high quality $PtSe_2$ films on bilayer graphene/6H(0001) substrate by using MBE method for the first time. The surface morphology of the as-prepared $PtSe_2$ on the surface of bilayer graphene is shown in Fig. 9e. The obtained $PtSe_2$ film is single crystalline and the thickness ranges from 1 to 22 layers.

The reliable production of 2D $PtSe_2$ with controlled structure is a prerequisite in exploring their properties and possible applications. As mentioned above, 2D $PtSe_2$ has been prepared by various approaches including mechanical exfoliation, CVD, CVT, TAC, and other methods. A comprehensive summary and comparison with these methods is presented in Table 1. The aforementioned methods have inherent disadvantages which make it difficult to achieve the large area and highly crystalline structure. And the synthesis of large lateral size and uniform monolayer or few-layer 2D $PtSe_2$ is still challenge. Moreover, the growth mechanism has yet to be clarified. Therefore, extended works need to be done to achieve the controllable synthesis of 2D $PtSe_2$.

5 Applications

5.1 Photodetectors

Photodetectors can directly convert optical signals to electrical signals. It has been widely applied in many fields such as optical communication, industrial automatic control, and military [147–149]. 2D materials, including graphene, BP, and TMDCs, are considered to be promising candidates for high-performance photodetectors due to their excellent properties and complementary metal oxide semiconductor compatible [147, 150–155]. However, it is still challenge to fabricate high responsivity 2D material-based photodetectors along with ultrafast response. Although group-6 TMDCs (such as MoS_2 and WS_2) have exhibited impressive optoelectronic properties [156–158], their photodetection performance is severely limited due to their relatively large band gap and low carrier mobility, especially in the IR range.

As newly emerged 2D materials, group-10 TMDCs have been widely studied as high-performance photodetectors [29, 117, 121, 159]. Among these group-10 TMDCs materials, $PtSe_2$ has been demonstrated to have excellent photoelectric and electrical properties. As introduced above, the band gap of monolayer and bilayer $PtSe_2$ is 1.2 and 0.21 eV, respectively [25]. Simulation results have revealed that only monolayer $PtSe_2$ has a sizeable band gap and $PtSe_2$ become semimetallic as the number of layers larger than three or four. Thus, 2D $PtSe_2$ is proposed as an excellent candidate for broadband photodetectors in the visible to mid-IR range [32, 33, 116–118, 120, 121, 123, 129, 160]. As shown in Table 2, the performance of $PtSe_2$-based photodetectors is summarized for comparison.

Table 2 Summary of $PtSe_2$-based photodetectors

| Materials	Wavelength (nm)	Photoresponsivity (mA W^{-1})	Rise/fall times (μs)	References
$PtSe_2$/CdTe	200–2000	506.5@780 nm	8.1/43.6	[121]
$PtSe_2$/Silicon	200–1550	12,650@780 nm	10.1/19.5	[160]
$PtSe_2$/GaAs	200–1200	262@808 nm	5.5/6.5	[120]
$PtSe_2$/Ge	1300–2200	602@1550 nm	7.4/16.7	[118]
$PtSe_2$/Perovskite	300–1200	117.7@808 nm	78/60	[123]
$PtSe_2$	360–2000	490@970 nm	–	[32]
$PtSe_2$/GaN	200–800	193@265 nm	45/402	[129]
$PtSe_2$/Si	200–1550	520@808 nm	55.3/170.5	[116]
$PtSe_2$	632-10^4	6250@632 nm	1.1/1.2×10^3	[33]
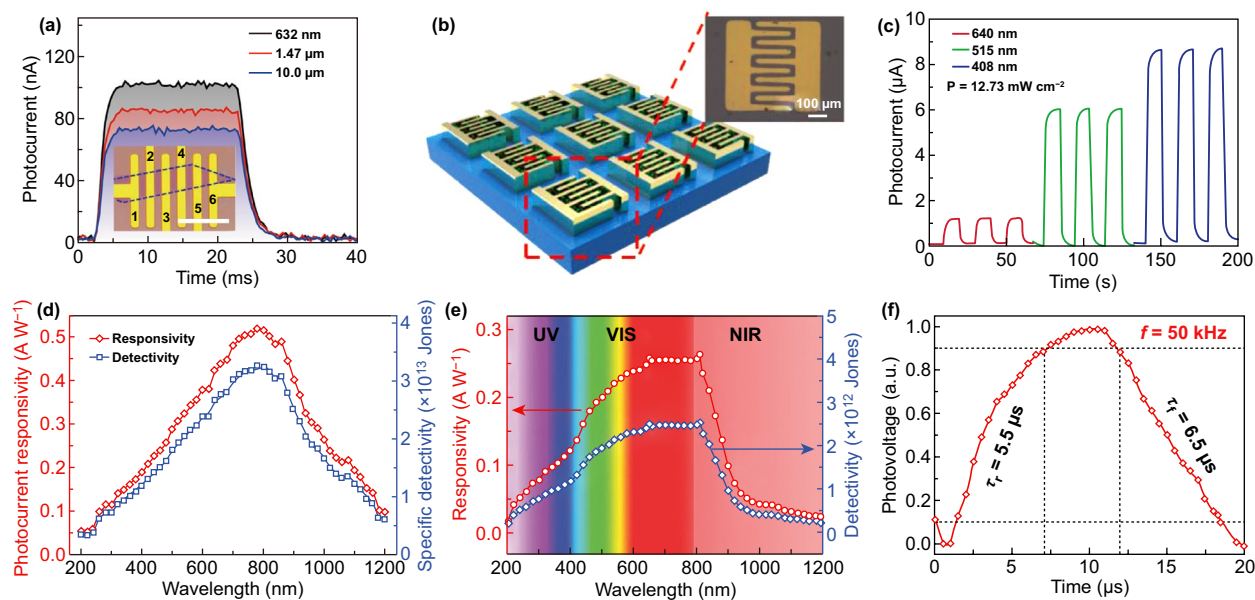
Fig. 10 Performance of PtSe$_2$-based photodetectors. **a** Time resolved photoresponse of the bilayer PtSe$_2$-based photodetectors; the inset is the microscopic image the device. Reproduced with permission [33]. Copyright 2018, Springer Nature. **b** Schematic structure and an optical microscopic image of the 2D PtSe$_2$ film-based photodetector. **c** Time resolved photocurrent of the photodetector as a response to light on/off at wavelengths of 408 nm, 515 nm, and 640 nm. **b, c** Reproduced with permission [55]. Copyright 2018, John Wiley and Sons. **d** Photocurrent responsivity and specific detectivity of the PtSe$_2$ film-based photodetector as functions of the wave length of the incident light. Reproduced with permission [116]. Copyright 2018, Royal Society of Chemistry. **e** Responsivity and detectivity of the PtSe$_2$/GaAs heterojunction as a function of wavelength. **f** A single normalized cycle measured at 50 kHz for estimating both response time (τ_r) and recovery time (τ_f). **e–f** Reproduced with permission [121]. Copyright 2018, John Wiley and Sons

Yu et al. investigated the photoresponse of FETs based on bilayer PtSe$_2$ in the wavelength range from 632 nm to 10 μm, as shown in Fig. 10a [33]. The photoresponsivity of 6.25 A W^{-1} and a rise time of about 1.2 ± 0.1 ms were achieved for 640 nm laser illumination. Moreover, the photoresponsivity in the near-IR (~ 1.47 μm) wavelength range and mid-IR (~ 10 μm) wavelength range is about 5.5 and 4.5 A W^{-1}, respectively. The fitted rise and fall time for the bilayer PtSe$_2$-based photodetector are much better than those 2D materials (such as BP, MoS$_2$, and MoSe$_2$)-based photodetectors [15, 147, 149, 150, 161–166]. These results indicate that 2D PtSe$_2$ is highly promising platforms for high sensitive and broadband optoelectronic application in the range of visible light to mid-IR wavelengths.

Su et al. investigated the performance of PtSe$_2$ film-based photodetector on SiO$_2$/Si [55]. The schematic structure of the photodetector device and the corresponding optical image are shown in Fig. 10b. As shown in Fig. 10c, the broadband photoresponse is demonstrated in the wavelengths range from 408 to 640 nm. When the photodetector was irradiated by 408 nm laser, the device exhibited the highest photoresponse with the photocurrent reaches 9 μA,

while the photocurrent was about ~ 6 and ~ 1 μA as irradiated by 640 and 510 nm laser, respectively. The corresponding photoresponsivity with incident power density of 12.73 mW cm^{-2} is 0.1A W^{-1} (at 640 nm), 0.25 A W^{-1} (at 515 nm), and 0.4 A W^{-1} (at 408 nm). Moreover, the PtSe$_2$ can be directly grown on a flexible polyimide substrate owing to the advantage of the low-temperature growth process. Su et al. [55] also fabricated a flexible photodetector based on PtSe$_2$ film on the polyimide substrate by using the same conditions of photodetectors fabricated on the SiO$_2$/Si substrate. The photodetector exhibits great stability under different bending radius with almost no degradation in the photocurrent even after 1000 bending cycles.

Yim et al. studied the photoresponse of the layered PtSe$_2$-based Schottky barrier diodes on *n*-type Si [32, 112]. The diode was fabricated by transferring PtSe$_2$ thin films onto the pre-patterned *n*-type Si substrate. The PtSe$_2$ film exhibits strong photoresponse over a broadband wavelength range of 360–2000 nm. The maximum photoresponsivity of 0.49 A W^{-1} and minimum photoresponsivity of 0.0001 A W^{-1} were measured at photon energies above and below the band gap of Si. In the visible region, the large part of

the photocurrent in the $PtSe_2$/Si device is generated in the Si layer, whereas the photocurrent in IR region is generated in the $PtSe_2$ layer [32]. Xie et al. and Zeng et al. in situ fabricated vertical $PtSe_2$/Si hybrid heterojunctions [33, 116]. The $PtSe_2$ films were grown directly on Si substrates, which can effectively avoid the interface contamination, structural continuity deterioration, and materials surface tear. This heterojunction-based photodetector is highly sensitive in a broad wavelength region from deep ultraviolet (200 nm) to near-IR (1550 nm). As shown in Fig. 10d, the highest photoresponsivity of the $PtSe_2$/Si can reach 0.52 A W^{-1} at 808 nm, and the specific detectivity and rise/fall response times are 3.26×10^{13} Jones and 55.3/170.5 µs [116]. When Si nanowires were chosen to fabricate $PtSe_2$/Si heterojunction, a high photoresponsivity of 12.65 A W^{-1} and very fast rise/fall time of 10.1/19.5 µs are obtained in the $PtSe_2$/Si nanowires-related photodetector [33].

The broad band gap range and high carrier mobility of $PtSe_2$ make it be an excellent candidate for developing high-performance photodetectors. However, the ultrathin thickness of 2D $PtSe_2$ materials result in a low absorption to incident light, leading to a small photocurrent, large dark current and low specific detectivity. In order to develop broadband, high sensitive, low power, and high photoresponsivity photodetector, $PtSe_2$-based heterostructure for optoelectronic applications has been studied [117, 118, 120, 121, 129]. Wu et al. [121] designed a vertical $PtSe_2$/CdTe heterojunction-based photodetector and this photodetector exhibited a broad detection wavelength range of 200–2000 nm. This heterojunction structure can enhance the absorption to near-IR light, as well as the improvement of response speed due to the formation of a built-in electric field. Zeng et al. [121] fabricated a $PtSe_2$/GaAs heterojunction on SiO_2/Si substrate via a deposition process and wet transfer process. The $PtSe_2$/GaAs heterojunction-based photodetector exhibited high sensitivity to broad wavelength range from 200 to 1200 nm. As shown in Fig. 10e, the photodetector exhibits peak sensitivity in
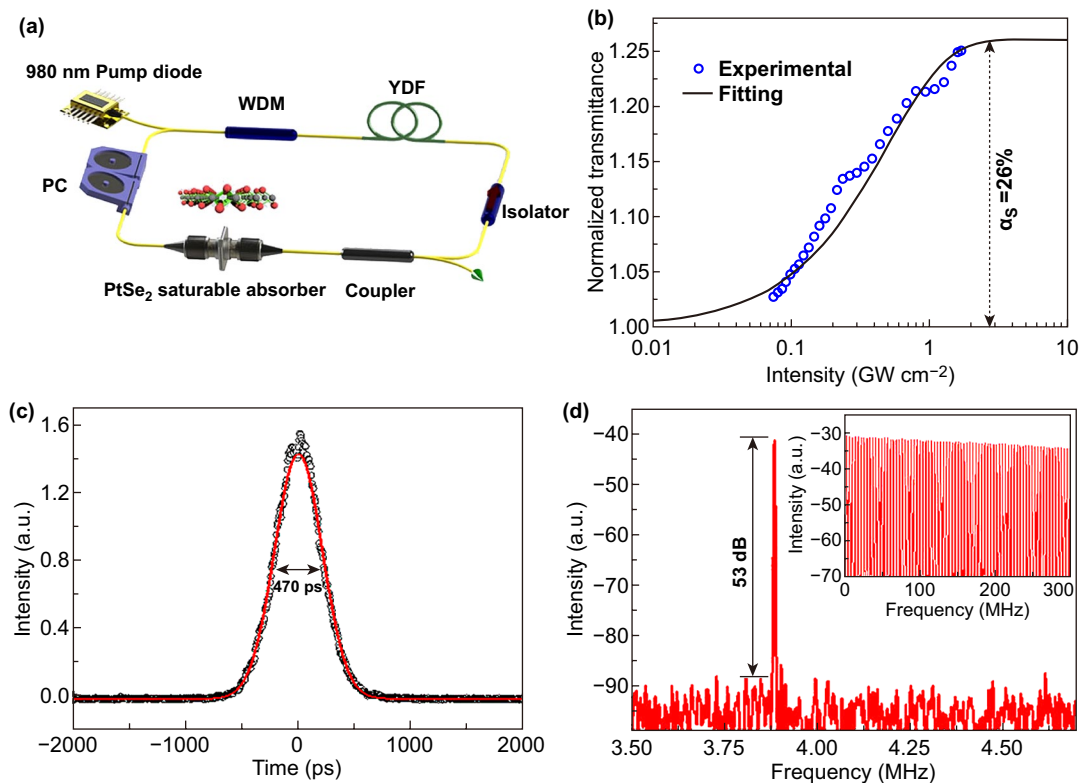

Fig. 11 Mode locker laser of $PtSe_2$. **a** Schematic diagram of the YDF laser ring cavity. PC: polarization controller. WDM: wavelength division multiplex. Isolator: polarization-independent isolator. YDF: ytterbium-doped fiber. **b** Nonlinear transmission curve of 10 nm $PtSe_2$ saturable absorber. **c** Single pulse profile indicates the pulse duration. **d** Radio-frequency spectrum of the mode-locked pulses and inset shows the corresponding wideband (0–300 MHz) radio-frequency spectrum. Reproduced with permission [177]. Copyright 2018, American Chemical Society

the range from 650 to 810 nm, which exclusively originates from the PtSe$_2$ layer. The rise/fall time for the photodetector is 5.5/6.5 μs (shown in Fig. 10f), which are faster than other state-of the art 2D materials (such as BP, MoS$_2$, WS$_2$, and graphene/Si heterojunction) photodetectors [167–170]. Wang et al. [118] fabricated a PtSe$_2$/Ge heterojunction-based photodetector, which is highly sensitive to the near-IR light. The photodetector device can operate without an external power supply due to the photovoltaic effect under the near-IR light illumination [112, 118, 120].

5.2 Mode-Locked Laser

The mode locking based on SA has been taken as the most important and efficient optical technique to generate ultrafast pulse laser from a continuous wave laser [171–176]. The mode-locked laser systems have been widely applied in areas including ultrafast pump sources, high-accuracy measurement, ultrafine laser micromachining, and laser surgery [171]. This technique exhibits many advantages such as low cost, high power scalability, high reliability, good mechanical stability, and excellent beam quality. 2D materials with saturable absorber properties have been widely utilized as saturable absorber in the laser cavity for ultrafast pulse generation.

In 2018, Yuan et al. [177] reported the SA properties of 2D PtSe$_2$ film for the first time. Figure 11a shows the schematic diagram of the experimental setup of the ytterbium-doped fiber (YDF) laser ring cavity. As shown in Fig. 11b, the NLO measurements results show that PtSe$_2$ film (about 10 nm) exhibits a large modulation depth up to 26% at the wavelength of 1064 nm with a lower saturable intensity, while the saturable intensity is as low as 0.316 GW cm^{-2}. The modulation depth refers to the maximum change of transmission or total amount of light loss by saturable absorption of the absorber. The relatively large modulation depth at the wavelength of 1064 nm indicates the potential of PtSe$_2$ to be an excellent nonlinear absorption material. As shown in Fig. 11c, d, the mode-locking performance of PtSe$_2$ film is investigated by transferring a PtSe$_2$ film onto the fiber tip. The mode-locked pulse centered at 1064.47 nm has the pulse duration of 470 ps.

Tao et al. [94] also reported the properties of the passively mode-locked solid state laser by using a 24-nm-thick PtSe$_2$ film as the saturable absorber. A pulse duration of 15.8 ps is obtained in the mode-locked fiber laser based on a PtSe$_2$ film coated fiber. Zhang et al. [95] fabricated and studied 1563 nm Er-doped fiber laser based on PtSe$_2$ film, with pulse duration of 1.02 ps and maximum single pulse energy of 0.53 nJ. Huang et al. [100] fabricated a femtosecond fiber mode locking by transferring thicker PtSe$_2$ (~ 73 nm) onto a D-shaped fiber. Due to the nonlinear modulation from the PtSe$_2$, the pulse duration of 861 fs and single-to-noise ratio of 61.1 dB were achieved for the 1567 nm mode-locking laser. The recent progresses on the PtSe$_2$-based mode-locking laser make PtSe$_2$ a promising 2D material for on-chip integration of GHz laser sources toward higher repetition rates and shorter pulse duration [31, 82, 84, 125].

5.3 Field Effect Transistors

One of the important applications of 2D PtSe$_2$ materials is the field effect transistors (FETs). The very first report on 2D layered PtSe$_2$ material for FETs was reported by Zhao et al. in 2017 [28]. The room temperature electron mobility of the few-layer PtSe$_2$ FETs device is 210 cm^2 V^{-1} s^{-1}, which is much smaller than the theoretically predicted value [28, 178]. Zhao et al. further studied the temperature-dependent mobility of PtSe$_2$ FETs and the mobility of few-layer PtSe$_2$ FETs (~ 11 nm). The field effect mobility and the gate-dependent mobility of the 11 nm-thick-PtSe$_2$ FETs are shown in Fig. 12a, b. The mobility of the PtSe$_2$ FETs in a back-gated configuration on SiO$_2$/Si increased from 210 to 414 cm^2 V^{-1} s^{-1}, as the temperature decreased from 300 to 100 K. Moreover, as the temperature continues to decrease to 25 K, the mobility of the PtSe$_2$ FETs decreased from 414 to 353 cm^2 V^{-1} s^{-1}. For comparison, the temperature-dependent mobility of a thinner few-layer PtSe$_2$ (~ 8 nm) FETs is measured. When the temperature increased from 25 to 300 K, the mobility increased from 149 cm^2 V^{-1} s^{-1} (at 25 K) to 233 cm^2 V^{-1} s^{-1} (at 125 K) and then decreased to 140 cm^2 V^{-1} s^{-1} (at 300 K). The variation of carrier mobility mainly ascribed to the layer-dependent band gap of PtSe$_2$. The reduced band gap of thicker PtSe$_2$ leads to the increased carrier density, which improves the screening of charge
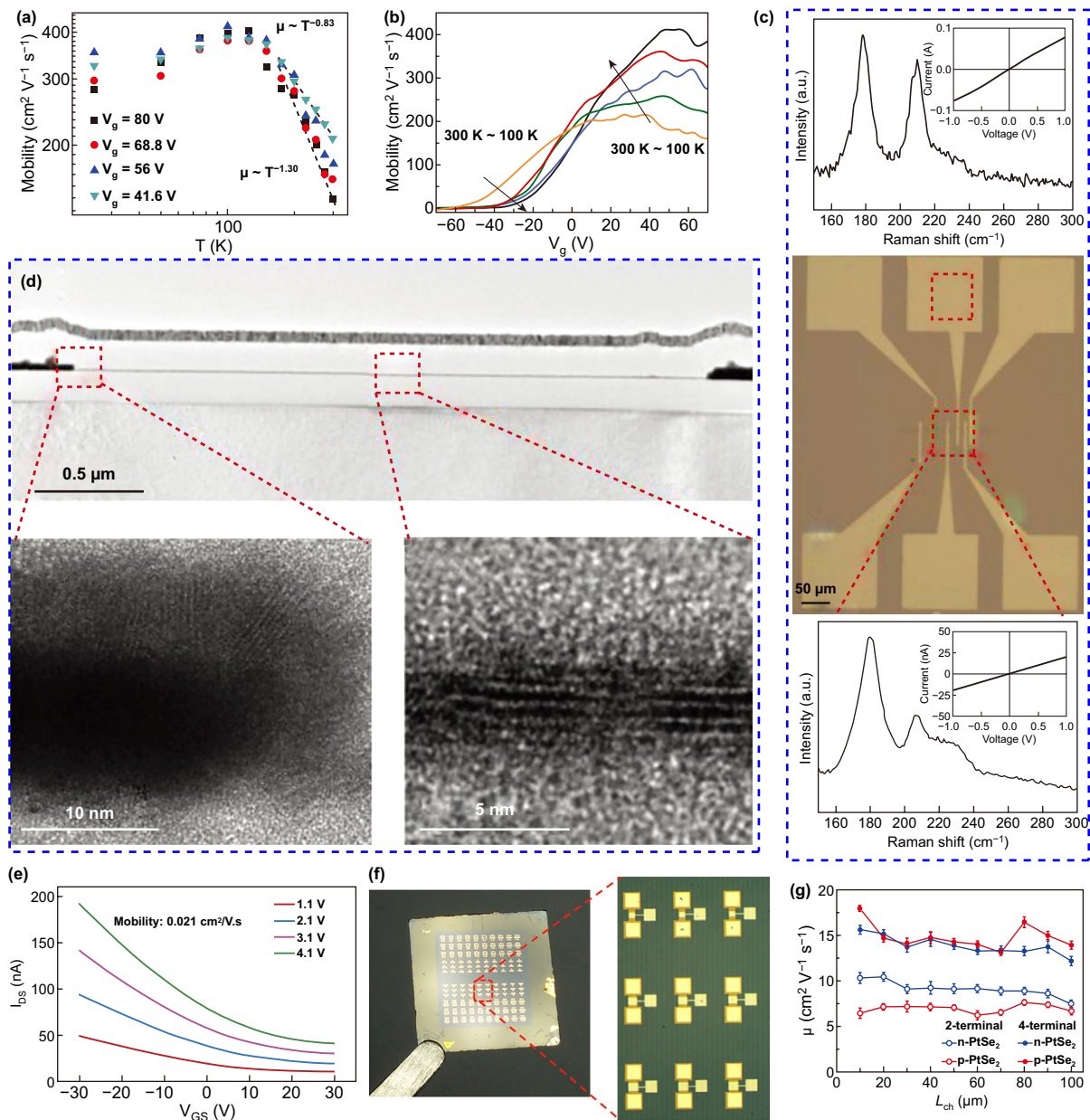
Fig. 12 Performance of 2D PtSe$_2$ FETs. **a** Temperature-dependent field effect electron mobility of an 11-nm-thick PtSe$_2$ FET. **b** Field effect electron mobility versus gate voltage at different the temperature (from 100 to 300 K). Reproduced with permission [28]. Copyright 2018, John Wiley and Sons. **c** An optical microscope image of all PtSe$_2$-based devices (middle) and the corresponding Raman spectra of the electrode (upper) and the channel (bottom) regions. **d** Cross-sectional TEM images corresponding to the all PtSe$_2$-based device shown in **c**. High magnification TEM images are an enlarge of the electrode (left) and channel (right) regions. **e** $I_D S$–$V_G S$ curves at different $V_D S$ (which are set as 1.1, 2.1, 3.1, and 4.1 V). Reproduced with permission [55]. Copyright 2018, John Wiley and Sons. **f** Optical microscopic images of an PtSe$_2$ FETs array. **g** Comparison of the two terminals and four-terminal mobility as a function of the channel length (L_{ch}) for p-type and n-type PtSe$_2$ film-based devices. Reproduced with permission [107]. Copyright 2019, John Wiley and Sons

impurities by the bottom layer. The conductivity and carrier mobility are thus significantly improved due to the carriers in the bottom layer can effectively suppress the Coulomb potential of the charge impurities at the interface [28, 179].

Previous theoretical and experimental results have demonstrated that the thinner PtSe$_2$ exhibits a semiconducting behavior, while the thicker PtSe$_2$ exhibits a metallic behavior [42, 55]. As shown in Fig. 12c, Su et al. [55] fabricated a

full PtSe$_2$ FETs wherein the thicker PtSe$_2$ (~ 50 nm) is used as the electrodes and the thinner PtSe$_2$ (~ 3 nm) is used as the channel materials. To further confirm the existence of the PtSe$_2$ in both the channel and electrode, Raman spectra and TEM images of the channel and electrode materials are presented in Fig. 12c, d. The measured electrical properties of the full PtSe$_2$ FETs are shown in Fig. 12e. The mobility of the full PtSe$_2$ FETs ranges from 0.007 to 0.021 cm^2 V^{-1} s^{-1}, which is lower than the device using pure Pt electrodes [55]. Yim et al. studied the effect of contact metals and edge contact at the metal/PtSe$_2$ interface to the transport characteristics of the FETs devices [113]. They found that by increasing the edge contact length, the contact resistivity was improved by up to 70% compared to devices with conventional top contacts, which provide a quick insight into the realization of high-performance opto/electronic devices. Ansari et al. fabricated a back-gated FETs device with different channel thickness [119]. The on/off ratio and carrier mobility are measured at room temperature. The I_{on}/I_{off} ratio of thinner PtSe$_2$ film (2.5–3 nm) FETs exceeds 230, while the I_{on}/I_{off} ratio of thicker PtSe$_2$ film (5–6.5 nm) FETs is sharply decreased to about 1.4. These variations are mainly due to the quantum confinement effect in the thin 2D PtSe$_2$ film. Xu et al. systematically studied the electrical properties of n-doping and p-doping PtSe$_2$ film by fabricating top-gated FET [107]. The optical microscopic image of an as-fabricated FETs array is shown in Fig. 12f. The I_{on}/I_{off} ratio of the PtSe$_2$ FETs is about 25 (n-type) and 40 (p-type). The channel length-dependent electrical properties of the PtSe$_2$ FETs have been studied, and the effective field effect mobility of different configurations is presented in Fig. 12g. The four-terminal field effect mobility is nearly three times higher than two terminal field effect mobility for the p-type PtSe$_2$, and two times higher than the n-type PtSe$_2$, respectively. Han et al. [114] further identified the interrelation of structural morphology and electrical transport in 2D PtSe$_2$ thin film by applying corroborating HR-TEM and FETs characterization. The highest mobility measured in this FETs device reached 625 cm^2 V^{-1} s^{-1}, which is among the highest experimentally measured mobility value reported for PtSe$_2$ FETs.

Besides the FETs devices on conventional rigid substrate, Okogbue et al. [180] fabricated a kirigami FETs on flexible polyimide substrate. By taking advantage of the low-temperature synthesis process, they fabricated integrated 2D PtSe$_2$ film on flexible. These 2D PtSe$_2$/polyimide kirigami patterns exhibit an extremely large stretchability of 2000% without compromising their intrinsic electrical conductance. The corresponding I_{ds}–V_g transfer characteristics from the kirigami FETs of varying stretch level (0%, 100%, and 200%) are measured, and these plots clearly reveal that p-type semiconducting transports are well retained with slightly decreasing I_{ds} during the increasing mechanical stretch.

Recently, impressive advances have been achieved for the fabrication of PtSe$_2$ FETs devices. The experimentally measured carrier mobility of PtSe$_2$ is much higher than the carrier mobility of group-6 2D TMDC materials, yet it is still much lower than the theoretically predicated value. For 2D materials, there are several extrinsic factors mainly dominating the charge transport, including structurally defects, charge impurity, surface optical phonon scattering, and surface traps [181–184]. These critical issues also existed in 2D PtSe$_2$-based device, the negative effects induced by the unexpected impurity (Se dopant), heterojunction interface (electrode/PtSe$_2$), and contact resistance still need to be overcome. Besides, due to the low-temperature synthesis process of large-scale 2D PtSe$_2$ film, it is would be interesting to develop high-performance flexible devices.

5.4 Photocatalysis

2D materials have been widely studied as high-performance photocatalyst due to its large specific area and excellent electronic properties [185–188]. In 2013, Zhuang et al. [40] performed a systematic theoretical study on the photocatalytic performance of monolayer TMDCs by using first principles calculation. As shown in Fig. 13a, the position of CBM and VBM of some monolayer 2D TMDCs at pH = 0 and 7 is summarized. According to the calculation results, PtSe$_2$, PtS$_2$, MoS$_2$, and WS$_2$ show potential for photocatalysis. Moreover, the solvation enthalpies (ΔHS_{olv}) of monolayer PtSe$_2$, PtS$_2$, MoS$_2$, and WS$_2$ are calculated, as shown in Fig. 13b. For both case of isolated and associated ions, the ΔHS_{olv} are significantly large than the value of HgS, which set as a reference. These calculation results indicate that these monolayer 2D TMDCs are insoluble and stable in aqueous solution, which make them ideal candidate for high-performance photocatalyst. The calculation results show that few-layer PtSe$_2$ exhibit great potential for high-performance photocatalysis due to the sizable band gap within the visible wavelength range.
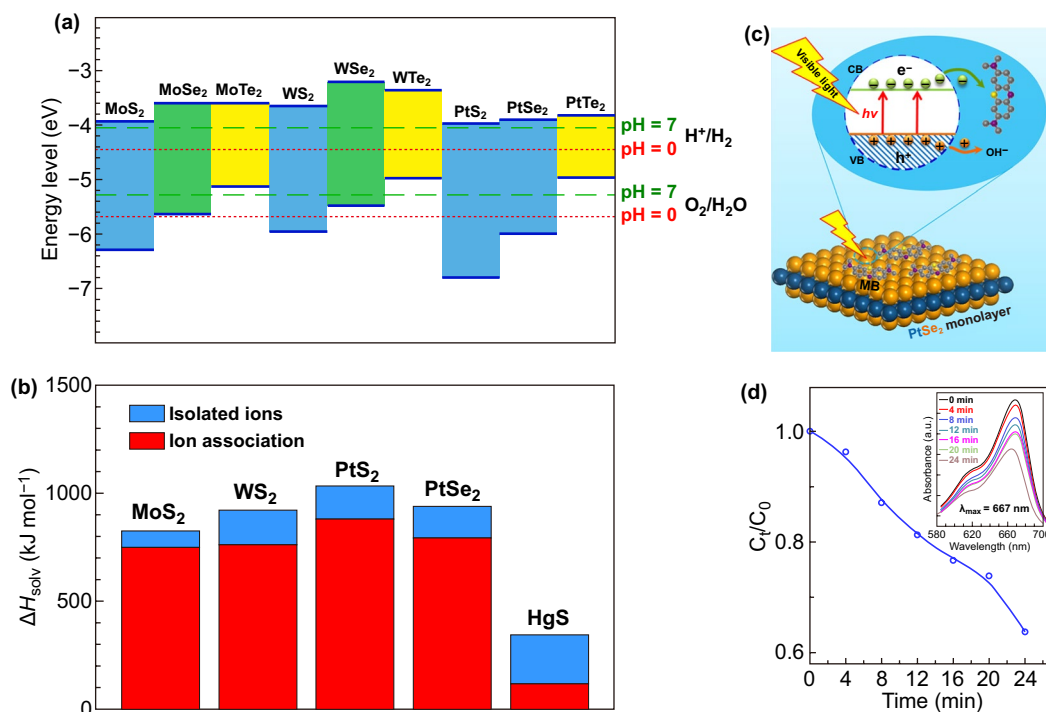
Fig. 13 Photocatalytic properties of PtSe$_2$. **a** CBM and VBM edge positions of monolayer TMDCs relative to the vacuum. **b** Comparison of the calculated solvation enthalpies (ΔHS_{olv}) of monolayer PtSe$_2$, PtS$_2$, MoS$_2$, and WS$_2$ to the value of HgS. The ΔHS_{olv} of insoluble HgS is shown for comparison which shows a negligible solubility of 1.27×10^{-27} mol/100 g of H$_2$O. Reproduced with permission [40]. Copyright 2019, American Chemical Society. **c** Schematic diagram of the photocatalytic degradation mechanism of methylene blue (MB) molecular over PtSe$_2$ film. **d** Relationship between C_t/C_0 and the photocatalytic degradation time under visible light (C_t and C_0 are the MB concentrations at time t and 0 min). The inset shows the UV–Vis absorption spectra of MB solution for every 4 min. Reproduced with permission [25]. Copyright 2015, American Chemical Society

Wang et al. [25] carried out a methylene blue photocatalytic degradation experiment to evaluate the photocatalytic property of PtSe$_2$ film. As shown in Fig. 13c, d, the schematic diagram of the photocatalytic degradation of methylene blue process and the time dependent photocatalytic degradation of methylene blue were evaluated by test the concentration of the methylene blue aqueous solution. It can be seen that almost 38% of methylene blue molecules are degraded in 24 min. As the PtSe$_2$ catalyst absorbed a photon, an active electron–hole pair generated and the absorbed methylene blue are degraded by the high energy photon excited electrons. For comparison, the monolayer PtSe$_2$ exhibits high photocatalytic degradation rate comparable with the nitrogen doped TiO$_2$ nanoparticles [189].

Sun et al. [127] fabricated a PtSe$_2$ film onto FTO substrate via TAC process and studied the solar-driven water splitting performance of the PtSe$_2$ film. The highest photocatalytic H$_2$ production rate can reach 506 mmol hm^{-1}. The photocatalytic activity of the PtSe$_2$/FTO thin film has no obvious

decrease in ambient and acidic/alkaline solution even after aging for 1 year. Moreover, the PtSe$_2$-based composite also shows high photocatalytic performance, such as PtSe$_2$/graphene [130, 131] and PtSe$_2$/TiO$_2$/graphene [131–133].

5.5 Hydrogen Evolution Reaction

Hydrogen has been recognized as the future energy carrier due to its ultrahigh energy density as a sustainable clean energy source [190, 191]. Experimental and theoretical efforts have indicated that 2D TMDCs materials can serve as ultrathin electrocatalysts for the hydrogen evolution reaction (HER) [38, 186, 192–195].

Chia et al. [196] studied the HER electro-catalytic properties of Pt dichalcogenides by performing DFT calculations. As shown in Fig. 14a, b, the PtSe$_2$ has over-potential of 0.63 eV and Tafel slop of 132 mV dec^{-1}. However, the HER performance of PtSe$_2$ can be further enhanced by both
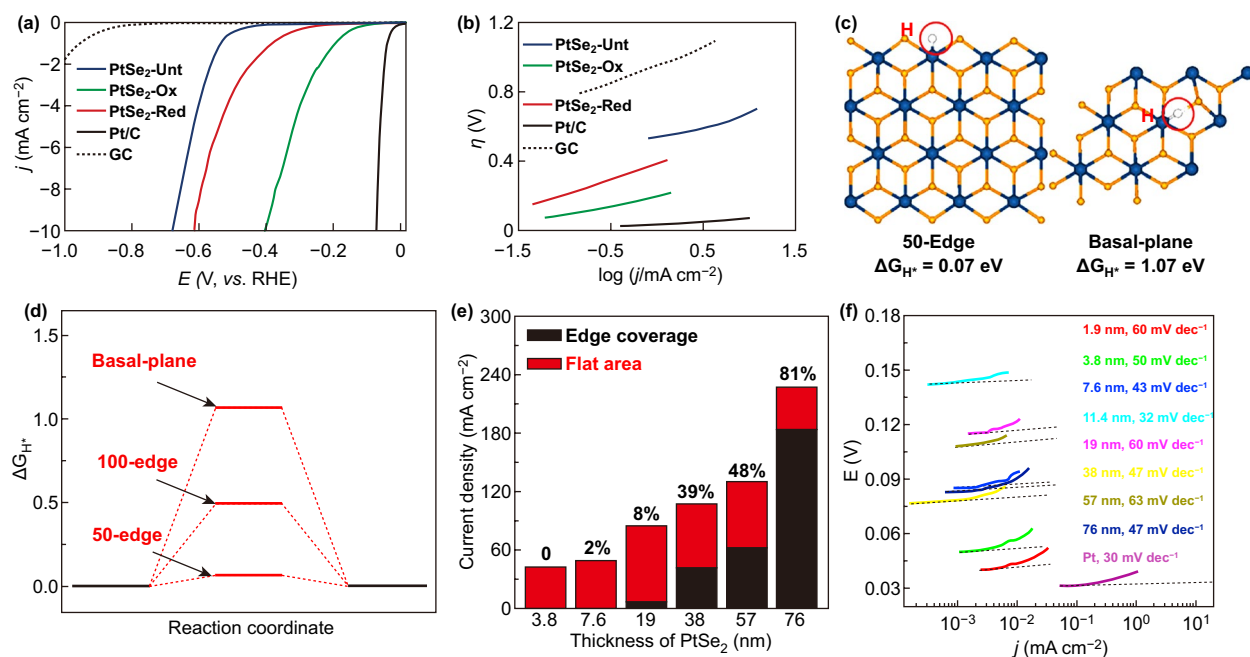
Fig. 14 HER properties of PtSe₂. **a** Linear sweep voltammograms versus the reversible hydrogen electrode (RHE) for HER on PtSe₂, electrochemically oxidized PtSe₂ and electrochemically reduced PtSe₂. **b** Tafel plot for PtSe₂, electrochemically oxidized PtSe₂ and electrochemically reduced PtSe₂. **a, b** Reproduced with permission [196]. Copyright 2016, John Wiley and Sons. **c** Density functional theory theoretical calculations of the H adsorption energies at the 50-edge and basal-plane of monolayer 1T-PtSe₂. White ball: H atom, Blue ball: Pt atom, and yellow ball: Se atom. **d** Gibbs free energies (ΔG_{H*}) diagram of different H adsorption states on 1T-PtSe₂. **c, d** Reproduced with permission [197]. Copyright 2019, American Chemical Society. **e** Relationship between the current density and edge sites density on the top surface of PtSe₂ film and the corresponding **f** Tafel plots. **e–f** Reproduced with permission [128]. Copyright 2017, Elsevier

reduction and oxidation process. For example, the oxidized PtSe₂ has over-potential of 0.36 eV and Tafel slop of 93 mV dec⁻¹. The HER performance for PtSe₂ is activated by both oxidation and reduction, and the oxidized and reduced PtSe₂ exhibited better HER efficiency by a 46% and 9% decline in over-potential, respectively. Wang et al. investigated the HER performance of CVD synthesized 2H-PtSe₂ and 1T-PtSe₂ single crystal nanosheets. The 2H-PtSe₂ shows the Tafel slope of 78 mV dec⁻¹, which is much higher than that of 1T-PtSe₂ (48 mV dec⁻¹) [106]. Due to the semimetallic structure, the 1T-PtSe₂ exhibits relatively higher electrochemical activity (lower Tafel slop and higher over-potential). Shi et al. also found that the monolayer or few-layer 1T-PtSe₂ can serve as high-performance HER catalyst, and a record high HER efficiency [197]. As shown in Fig. 14c, d, the catalytic activity of monolayer 1T-PtSe₂ was calculated by DFT to identify the electrocatalytically active sites. The calculated Gibbs free energy (ΔG_{H*}) values of H adsorption at the 50-edge, 100-edge, and basal planes of the monolayer 1T-PtSe₂ are 0.07, 0.50, and 1.07 eV, respectively.

The relatively low ΔG_{H*} values for H adsorption at the edges indicate that the catalytically active sites mainly sit at the domain edges of 1T-PtSe₂. Besides, the lower Gibbs free energy values endow the monolayer 1T-PtSe₂ with excellent HER activity.

In 2017, Lin et al. proposed a facile strategy to synthesize edge rich PtSe₂ film with controlled edge density and make it possible to systematic study the relationship between the edge density and the HER performance [128]. A linear relationship between the edge density and the current density on the top surface of PtSe₂ film is established, as shown in Fig. 14e. As shown in Fig. 14f, the Tafel slope of PtSe₂ with different thickness ranging from 32 to 63 mV dec⁻¹ can be found. The current density increases with the edge density increases, which suggested that the edge density plays a key role in enhancing the HER activity of PtSe₂.

The HER performance of PtSe₂ has been experimentally and theoretically studied in the past few years. It has been revealed that the number of layers, edge density, and defect engineering play a key role in enhancing the HER activity
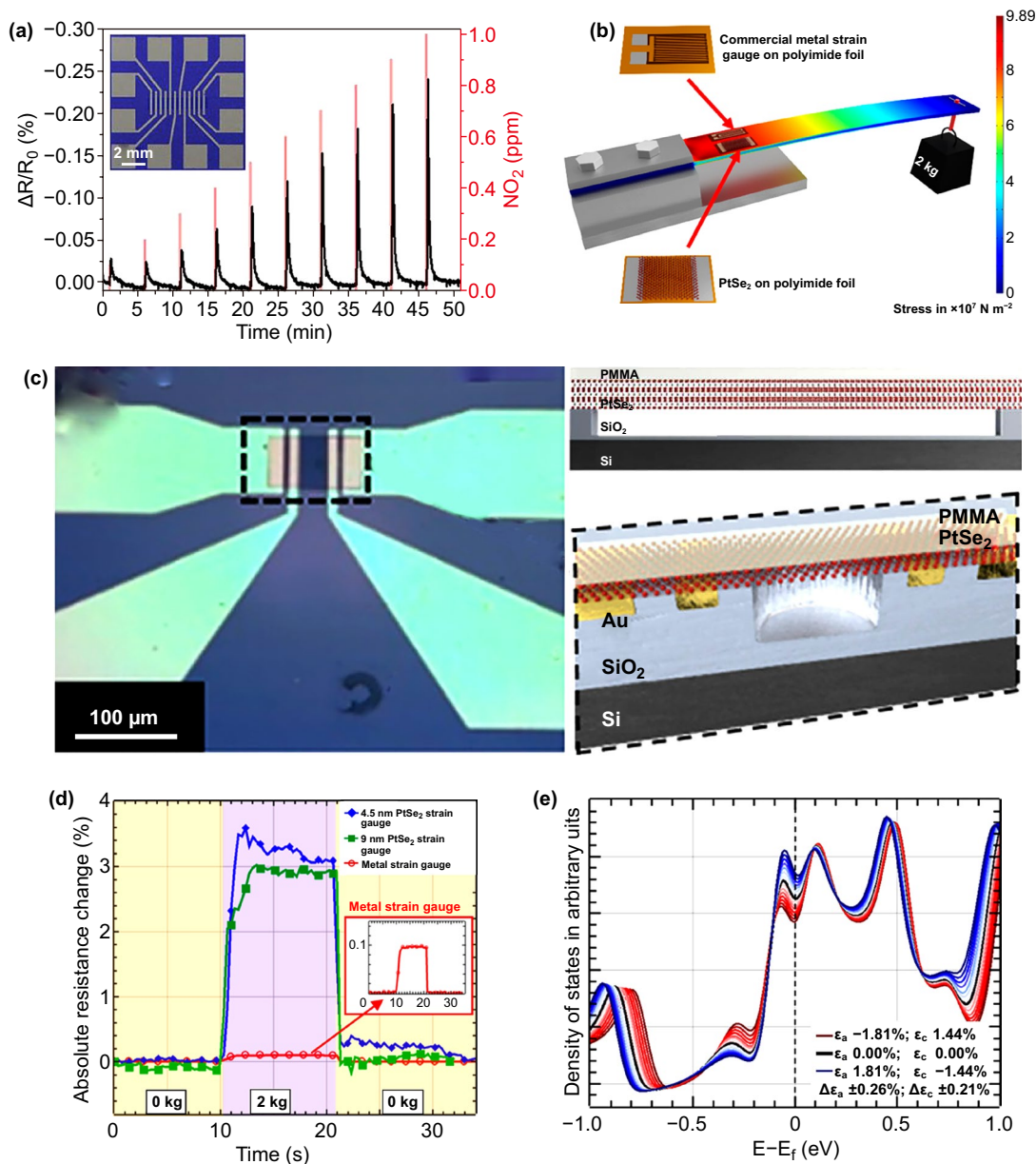
Fig. 15 Performance of 2D PtSe₂-based Sensors. **a** Gas sensor response of PtSe₂ film upon periodic NO₂ gas (0.1 to 1 ppm) exposure versus time with a bias voltage of 1 V. Red line indicates NO₂ gas injections, and black line indicates the resistance change. Inset shows an optical microscopic image of a contacted sensor device. Reproduced with permission [112]. Copyright 2016, American Chemical Society. **b** Bending beam setup with applied PtSe₂ film and commercially available metal strain gauges including stress simulation with the applied weight. **c** Optical microscopic image (left) of the pressure sensors with the PtSe₂ channel across the cavity area. Structure diagram (right) of the cross section of the cavity area with suspended PtSe₂ film. **d** Measured resistance changes during the measurement against time **e** Effect of the applied interlayer tensile strain (ε_a) and compression (ε_c) on the density of states close to the Fermi level. **b–e** Reproduced with permission [122]. Copyright 2018, American Chemical Society

of PtSe₂ [38, 142, 196–198]. However, the relationship between the structure, electronic structure, and HER activity of 2D PtSe₂ still is not elucidated, and the batch production of 2D metallic PtSe₂ is still not controllable enough in experimental.

5.6 Sensors

Sensors are a kind of integrated circuit devices that detect a specific physical parameter (gas, pressure, motion, moisture, etc.) and convert it to an electrical signal. Theoretical

simulation is a very effective approach to analyze and predict gas sensing properties of 2D PtSe$_2$ materials. In 2017, Sajjad et al. [199] conducted a systematically theoretical study on the absorption of various gases molecules on monolayer PtSe$_2$ by using first principles calculations. The adsorption energy, relaxed height, charge density differences, and electronic structure of monolayer PtSe$_2$ with absorbed CO, CO$_2$, H$_2$O, NH$_3$, NO, and NO$_2$ molecules were calculated, and the results indicate that sensors based on 2D PtSe$_2$ posse superior gas detection sensitivity. Chen et al. [200] investigated the response of a simulated monolayer PtSe$_2$-based gas sensor to the five types of SF6 decompositions (HF, H$_2$S, SO$_2$, So$_2$F$_2$, and SOF$_2$) by using the first principles study. The sensor shows rapid and intense response to the SF6 decomposition molecular, and it could be controlled by regulating the bias voltage. Moreover, theoretical simulation suggested that the gas sensitivity of PtSe$_2$ can be further enhanced by the *p*-type dopants of Ge and As [201].

Besides the theoretical simulation, also some experimental achievements have been reported. Figure 15a shows the PtSe$_2$ film-based gas sensors and its response to periodic NO$_2$ gas [112]. As the PtSe$_2$ film exposed to a 100 sccm flow of NO$_2$ mixture with N$_2$ carrier gas, an immediately response time upon to 10 s was measured. The resistance change, transient response/recovery time as a function of NO$_2$ concentration at a certain exposure time was further tested. The sensors exhibit ultrafast response/recover speed at room temperature. Moreover, 100 ppb of NO$_2$ can be detected at room temperature and the theoretical limit of detection is estimated to be a few parts per billion. The detection limit, sensitivity, responses/recovery time of 2D PtSe$_2$ gas sensors is much better than other 2D materials, such as graphene, MoS$_2$, MoSe$_2$, and MoTe$_2$ [202–205].

The unique structural and electronic properties of 2D PtSe$_2$ also make it a promising material for pressure sensors. As shown in Fig. 15b, c, centimeter-scale PtSe$_2$ films with thickness of 4.5 and 9 nm were synthesized and used to fabricate pressure sensors [122]. The sensitivity of the PtSe$_2$ film-based sensors can reach 1.05×10^{-1} mbar^{-1}, which is much better than other low-dimensional materials-based pressure sensors [206–210]. As shown in Fig. 15d, the piezo-resistive gauge factor of PtSe$_2$ film was measured by using a bending beam setup, and a negative gauge factor of -84.8 was obtained for the PtSe$_2$ film. According to the DFT calculation in Fig. 15e, an increase in DOS at Fermi level is observed for the in-plane stretching and out-of-plane compression, leading to a decrease in resistance under the applied stains and ascribe to the negative gauge factor. Moreover, Boland et al. [41] further demonstrated that the growth temperature and thickness of the PtSe$_2$ film have a great effect to the performance of the PtSe$_2$-based strain gauges. They found that the PtSe$_2$-based pressure sensors show strong response to high frequency mechanical vibrations. By attaching a film to a speaker, a strong resistance changes of PtSe$_2$/Polyimide film, with high signal-to-noise, is seen for to vibrations with frequencies of 95, 190, and 380 Hz were observed. These achievements suggest PtSe$_2$ as a very promising candidate for future micro- and nano-electromechanical systems applications.

6 Conclusions and Perspectives

During the last decades, the newly emerged 2D PtSe$_2$ has exhibited noticeable intrinsic nature and has experienced a remarkable development in theoretical and experimental. The most recent advances of 2D PtSe$_2$ including structure (crystal structure and electronic structure), properties (phase transition, vibration spectroscopic modes, and optical properties), synthesis methods (CVD, CVT, TAC, MBE, CVT, and sol–gel solution process), and potential applications (photodetectors, mode-locked laser, field effect transistors, photocatalytic, hydrogen evolution reaction, and sensors) are reviewed in this review. Although a tremendous progress has been achieved in the past few years, there are still some remaining especially for their practical application. Here, some major perspectives on the key challenges and the potential research directions are suggested to address these issues.

1. In order to fulfill the using demands for both fundamental studies and practical applications, more efficient and controllable synthesis methods should be developed. Previous study of graphene and TMDCs has inspired us that CVD is one of the most promising methods to grow 2D materials. However, the CVD growth of 2D PtSe$_2$ is still in its infancy. More compressive works about CVD should be developed to grow high quality single crystal 2D PtSe$_2$ with controlled thickness, lateral size, and defects, which is prerequisite for further understanding the optoelectronic properties of PtSe$_2$. Besides, in order to fulfill the demand of industrialization, highly efficient

synthetic approaches should be proposed to synthesize a mass of high quality 2D PtSe$_2$.

2. 2D PtSe$_2$ has been theoretically predicted to be a promising candidate to fabricate high-performance electronic and optoelectronic devices [211–224]. Although some pioneer works have been reported, the performance of 2D PtSe$_2$-based devices are stills much lower than theoretical prediction. Due to the layer-dependent band gap of 2D PtSe$_2$, photodetector based on 2D PtSe$_2$ may have excellent performance in a broadband from visible light to mid-IR. Vertical or lateral heterostructure based on 2D PtSe$_2$ may bring some novel properties, which have been proved in graphene and TMDCs.

3. Theoretical studies have demonstrated that the 2D PtSe$_2$ possesses excellent thermoelectric properties [67, 225, 226]. However, related experimental works are still lacking. The development of 2D PtSe$_2$-based flexible film or nanostructured thermoelectric materials may provide great opportunities for fabricating highly efficient thermoelectric devices.

4. 2D Janus materials have attracted extensive attentions due to their unique structure, electronic, and optoelectronic properties [227–229]. The formation of Janus crystal structure broke the inversion and mirror symmetry, leading to an intrinsic built-in electric field. Janus monolayer 2D materials with sandwiched structure may induce remarkable influence on their carrier mobility, band gap, and optical properties. Theoretical simulations reveal that Janus monolayer PtSSe may have great potential in optoelectronics and thermal management communities. However, related experimental studies are still lacking. It is still challenging to synthesize Janus monolayer PtSSe materials and study their fundamental properties.

References

1. K.S. Novoselov, A.K. Geim, S.V. Morozov, D. Jiang, Y. Zhang et al., Electric field effect in atomically thin carbon films. Science **306**(5696), 666–669 (2004). https://doi.org/10.1126/science.1102896

2. C.N.R. Rao, A.K. Sood, K.S. Subrahmanyam, A. Govindaraj, Graphene: The new two-dimensional nanomaterial. Angew. Chem. Int. Ed. **48**(42), 7752–7777 (2009). https://doi.org/10.1002/anie.200901678

3. H. Liu, A.T. Neal, Z. Zhu, Z. Luo, X. Xu, D. Tomanek, P.D. Ye, Phosphorene: an unexplored 2D semiconductor with a high hole mobility. ACS Nano **8**(4), 4033–4041 (2014). https://doi.org/10.1021/nn501226z

4. K.S. Novoselov, D. Jiang, F. Schedin, T.J. Booth, V.V. Khotkevich, S.V. Morozov, A.K. Geim, Two-dimensional atomic crystals. Proc. Natl. Acad. Sci. USA **102**(30), 10451–10453 (2005). https://doi.org/10.1073/pnas.0502848102

5. A.H. Castro Neto, F. Guinea, N.M.R. Peres, K.S. Novoselov, A.K. Geim, The electronic properties of graphene. Rev. Mod. Phys. **81**(1), 109–162 (2009). https://doi.org/10.1103/RevModPhys.81.109

6. J. Pei, J. Yang, T. Yildirim, H. Zhang, Y. Lu, Many-body complexes in 2D semiconductors. Adv. Mater. **3**(2), 1706945 (2019). https://doi.org/10.1002/adma.201706945

7. M. Luo, T. Fan, Y. Zhou, H. Zhang, L. Mei, 2D black phosphorus-based biomedical applications. Adv. Funct. Mater. **29**(13), 1808306 (2019). https://doi.org/10.1002/adfm.201808306

8. S.Z. Butler, S.M. Hollen, L. Cao, Y. Cui, J.A. Gupta et al., Progress, challenges, and opportunities in two-dimensional materials beyond graphene. ACS Nano **7**(4), 2898–2926 (2013). https://doi.org/10.1021/nn400280c

9. Q.H. Wang, K. Kalantar-Zadeh, A. Kis, J.N. Coleman, M.S. Strano, Electronics and optoelectronics of two-dimensional transition metal dichalcogenides. Nat. Nanotechnol. **7**(11), 699–712 (2012). https://doi.org/10.1038/nnano.2012.193

10. H. Mu, Z. Wang, J. Yuan, S. Xiao, C. Chen et al., Graphene-Bi$_2$Te$_3$ heterostructure as saturable absorber for short pulse generation. ACS Photonics **2**(7), 832–841 (2015). https://doi.org/10.1021/acsphotonics.5b00193

11. Z. Luo, D. Wu, B. Xu, H. Xu, Z. Cai et al., Two-dimensional material-based saturable absorbers: towards compact visible-wavelength all-fiber pulsed lasers. Nanoscale **8**(2), 1066–1072 (2016). https://doi.org/10.1039/c5nr06981e

12. J. Zheng, H. Zhang, S. Dong, Y. Liu, C.T. Nai et al., High yield exfoliation of two-dimensional chalcogenides using

sodium naphthalenide. Nat. Commun. **5**, 2995 (2014). https://doi.org/10.1038/ncomms3995

13. J. Liu, Z. Hu, Y. Zhang, H.-Y. Li, N. Gao et al., MoS$_2$ nanosheets sensitized with quantum dots for room-temperature gas sensors. Nano-Micro Lett. **12**(1), 59 (2020). https://doi.org/10.1007/s40820-020-0394-6

14. D. Li, Y. Gong, Y. Chen, J. Lin, Q. Khan, Y. Zhang, Y. Li, H. Zhang, H. Xie, Recent progress of two-dimensional thermoelectric materials. Nano-Micro Lett. **12**(1), 36 (2020). https://doi.org/10.1007/s40820-020-0374-x

15. Z. Kang, Y. Cheng, Z. Zheng, F. Cheng, Z. Chen et al., MoS$_2$-based photodetectors powered by asymmetric contact structure with large work function difference. Nano-Micro Lett. **11**(1), 34 (2019). https://doi.org/10.1007/s40820-019-0262-4

16. K. Khan, A.K. Tareen, M. Aslam, R. Wang, Y. Zhang et al., Recent developments in emerging two-dimensional materials and their applications. J. Mater. Chem. C **8**(2), 387–440 (2020). https://doi.org/10.1039/c9tc04187g

17. B. Wen, Y. Zhu, D. Yudistira, A. Boes, L. Zhang et al., Ferroelectric-driven exciton and trion modulation in monolayer molybdenum and tungsten diselenides. ACS Nano **13**(5), 5335–5343 (2019). https://doi.org/10.1021/acsnano.8b09800

18. C. Tan, H. Zhang, Two-dimensional transition metal dichalcogenide nanosheet-based composites. Chem. Soc. Rev. **44**(9), 2713–2731 (2015). https://doi.org/10.1039/c4cs00182f

19. H. Schmidt, F. Giustiniano, G. Eda, Electronic transport properties of transition metal dichalcogenide field-effect devices: surface and interface effects. Chem. Soc. Rev. **44**(21), 7715–7736 (2015). https://doi.org/10.1039/c5cs00275c

20. Y. Shi, H. Li, L.J. Li, Recent advances in controlled synthesis of two-dimensional transition metal dichalcogenides via vapour deposition techniques. Chem. Soc. Rev. **44**(9), 2744–2756 (2015). https://doi.org/10.1039/c4cs00256c

21. S. Syama, P.V. Mohanan, Comprehensive application of graphene: emphasis on biomedical concern. Nano-Micro Lett. **11**(1), 6 (2019). https://doi.org/10.1007/s40820-019-0237-5

22. M. Chhowalla, H.S. Shin, G. Eda, L.J. Li, K.P. Loh, H. Zhang, The chemistry of two-dimensional layered transition metal dichalcogenide nanosheets. Nat. Chem. **5**(4), 263–275 (2013). https://doi.org/10.1038/nchem.1589

23. L. Pi, L. Li, K. Liu, Q. Zhang, H. Li, T. Zhai, Recent progress on 2D noble-transition-metal dichalcogenides. Adv. Funct. Mater. **29**(51), 1904932 (2019). https://doi.org/10.1002/adfm.201904932

24. A.D. Oyedele, S. Yang, L. Liang, A.A. Puretzky, K. Wang et al., PdSe$_2$: pentagonal two-dimensional layers with high air stability for electronics. J. Am. Chem. Soc. **139**(40), 14090–14097 (2017). https://doi.org/10.1021/jacs.7b04865

25. Y. Wang, L. Li, W. Yao, S. Song, J.T. Sun et al., Monolayer PtSe$_2$, a new semiconducting transition-metal-dichalcogenide, epitaxially grown by direct selenization of Pt. Nano Lett. **15**(6), 4013–4018 (2015). https://doi.org/10.1021/acs.nanolett.5b00964

26. W.L. Chow, P. Yu, F. Liu, J. Hong, X. Wang et al., High mobility 2D palladium diselenide field-effect transistors with tunable ambipolar characteristics. Adv. Mater. **29**(21), 1602969 (2017). https://doi.org/10.1002/adma.201602969

27. I. Setiyawati, K.R. Chiang, H.M. Ho, Y.H. Tang, Distinct electronic and transport properties between 1T-HfSe$_2$ and 1T-PtSe$_2$. Chin. J. Phys. **62**, 151–160 (2019). https://doi.org/10.1016/j.cjph.2019.09.029

28. Y.D. Zhao, J.S. Qiao, Z.H. Yu, P. Yu, K. Xu et al., High-electron-mobility and air-stable 2D layered PtSe$_2$ FETs. Adv. Mater. **29**(5), 1604230 (2017). https://doi.org/10.1002/adma.201604230

29. D. Wu, J. Guo, J. Du, C. Xia, L. Zeng et al., Highly polarization-sensitive, broadband, self-powered photodetector based on graphene/PdSe$_2$/germanium heterojunction. ACS Nano **13**(9), 9907–9917 (2019). https://doi.org/10.1021/acsnano.9b03994

30. D. Wu, C. Jia, F. Shi, L. Zeng, P. Lin et al., Mixed-dimensional PdSe$_2$/SiNWA heterostructure based photovoltaic detectors for self-driven, broadband photodetection, infrared imaging and humidity sensing. J. Mater. Chem. A **8**(7), 3632–3642 (2020). https://doi.org/10.1039/c9ta13611h

31. G.Z. Wang, K.P. Wang, N. McEvoy, Z.Y. Bai, C.P. Cullen et al., Ultrafast carrier dynamics and bandgap renormalization in layered PtSe$_2$. Small **15**(34), 1902728 (2019). https://doi.org/10.1002/smll.201902728

32. C. Yim, N. McEvoy, S. Riazimehr, D.S. Schneider, F. Gity et al., Wide spectral photoresponse of layered platinum diselenide-based photodiodes. Nano Lett. **18**(3), 1794–1800 (2018). https://doi.org/10.1021/acs.nanolett.7b05000

33. X. Yu, P. Yu, D. Wu, B. Singh, Q. Zeng et al., Atomically thin noble metal dichalcogenide: a broadband mid-infrared semiconductor. Nat. Commun. **9**(1), 1545 (2018). https://doi.org/10.1038/s41467-018-03935-0

34. H.Q. Huang, S.Y. Zhou, W.H. Duan, Type-II Dirac fermions in the PtSe$_2$ class of transition metal dichalcogenides. Phys. Rev. B **94**(12), 121117 (2016). https://doi.org/10.1103/PhysRevB.94.121117

35. A. Avsar, A. Ciarrocchi, M. Pizzochero, D. Unuchek, O.V. Yazyev, A. Kis, Defect induced, layer-modulated magnetism in ultrathin metallic PtSe$_2$. Nat. Nanotechnol. **14**(7), 674–678 (2019). https://doi.org/10.1038/s41565-019-0467-1

36. M.A.U. Absor, I. Santoso, A. Harsojo, K. Abraha, H. Kotaka, F. Ishii, M. Saito, Strong Rashba effect in the localized impurity states of halogen-doped monolayer PtSe$_2$. Phys. Rev. B **97**(20), 205138 (2018). https://doi.org/10.1103/PhysRevB.97.205138

37. K.N. Zhang, M.Z. Yan, H.X. Zhang, H.Q. Huang, M. Arita et al., Experimental evidence for type-II Dirac semimetal in PtSe$_2$. Phys. Rev. B **96**(12), 125102 (2017). https://doi.org/10.1103/PhysRevB.96.125102

38. C. Tsai, K. Chan, J.K. Norskov, F. Abild-Pedersen, Theoretical insights into the hydrogen evolution activity of layered transition metal dichalcogenides. Surf. Sci. **640**, 133–140 (2015). https://doi.org/10.1016/j.susc.2015.01.019

39. M. Zulfiqar, G. Li, Y.C. Zhao, S. Nazir, J. Ni, Versatile electronic and magnetic properties of chemically doped 2D platinum diselenide monolayers: a first-principles study. AIP Adv. **7**(12), 125126 (2017). https://doi.org/10.1063/1.5011054

40. H.L.L. Zhuang, R.G. Hennig, Computational search for single-layer transition-metal dichalcogenide photocatalysts. J. Phys. Chem. C **117**(40), 20440–20445 (2013). https://doi.org/10.1021/jp405808

41. C.S. Boland, C.O. Coileain, S. Wagner, J.B. McManus, C.P. Cullen et al., $PtSe_2$ grown directly on polymer foil for use as a robust piezoresistive sensor. 2D Mater. **6**(4), 045029 (2019). https://doi.org/10.1088/2053-1583/ab33a1

42. A. Ciarrocchi, A. Avsar, D. Ovchinnikov, A. Kis, Thickness-modulated metal-to-semiconductor transformation in a transition metal dichalcogenide. Nat. Commun. **9**(1), 919 (2018). https://doi.org/10.1038/s41467-018-03436-0

43. M.Z. Yan, E.Y. Wang, X. Zhou, G.Q. Zhang, H.Y. Zhang et al., High quality atomically thin $PtSe_2$ films grown by molecular beam epitaxy. 2D Mater. **4**(4), 045015 (2017). https://doi.org/10.1088/2053-1583/aa8919

44. S. Wu, K.S. Hui, K.N. Hui, 2D black phosphorus: from preparation to applications for electrochemical energy storage. Adv. Sci. **5**(5), 1700491 (2018). https://doi.org/10.1002/advs.201700491

45. S. Kuriakose, T. Ahmed, S. Balendhran, V. Bansal, S. Sriram, M. Bhaskaran, S. Walia, Black phosphorus: ambient degradation and strategies for protection. 2D Mater. **5**(3), 139–146 (2018). https://doi.org/10.1088/2053-1583/aab810

46. V. Eswaraiah, Q. Zeng, Y. Long, Z. Liu, Black phosphorus nanosheets: synthesis, characterization and applications. Small **12**(26), 3480–3502 (2016). https://doi.org/10.1002/smll.201600032

47. F. Gronvold, E. Rost, On the sulfides, selenides and tellurides of palladium. Acta Chem. Scand. **10**(10), 1620–1634 (1956). https://doi.org/10.3891/acta.chem.scand.10-1620

48. A. Kjekshus, F. Gronvold, High temperature x-ray study of the thermal expansion of PtS_2, $PtSe_2$, $PtTe_2$ and $PdTe_2$. Acta Chem. Scand. **13**(9), 1767–1774 (1959). https://doi.org/10.3891/acta.chem.scand.13-1767

49. F. Gronvold, H. Haraldsen, A. Kjekshus, On the sulfides, selenides and tellurides of platinum. Acta Chem. Scand. **14**(9), 1879–1893 (1960). https://doi.org/10.3891/acta.chem.scand.14-1879

50. Y.D. Zhao, J.S. Qiao, P. Yu, Z.X. Hu, Z.Y. Lin et al., Extraordinarily strong interlayer interaction in 2D layered PtS_2. Adv. Mater. **28**(12), 2399–2407 (2016). https://doi.org/10.1002/adma.201504572

51. G. Guo, W. Liang, The electronic structures of platinum dichalcogenides: PtS_2, $PtSe_2$ and $PtTe_2$. J. Phys. C **19**(7), 995–1008 (1986). https://doi.org/10.1088/0022-3719/19/7/011

52. P.F. Li, L. Li, X.C. Zeng, Tuning the electronic properties of monolayer and bilayer $PtSe_2$ via strain engineering. J. Mater. Chem. C **4**(15), 3106–3112 (2016). https://doi.org/10.1039/c6tc00130k

53. C. Tan, X. Cao, X.J. Wu, Q. He, J. Yang et al., Recent advances in ultrathin two-dimensional nanomaterials. Chem. Rev. **117**(9), 6225–6331 (2017). https://doi.org/10.1021/acs.chemrev.6b00558

54. S. Manzeli, D. Ovchinnikov, D. Pasquier, O.V. Yazyev, A. Kis, 2D transition metal dichalcogenides. Nat. Rev. Mater. **2**(8), 17033 (2017). https://doi.org/10.1038/natrevmats.2017.33

55. T.Y. Su, H. Medina, Y.Z. Chen, S.W. Wang, S.S. Lee et al., Phase-engineered $PtSe_2$ -Layered films by a plasma-assisted selenization process toward all $PtSe_2$ -Based field effect transistor to highly sensitive, flexible, and wide-spectrum photoresponse photodetectors. Small **14**(19), e1800032 (2018). https://doi.org/10.1002/smll.201800032

56. W. Yao, E.Y. Wang, H.Q. Huang, K. Deng, M.Z. Yan et al., Direct observation of spin-layer locking by local Rashba effect in monolayer semiconducting $PtSe_2$ film. Nat. Commun. **8**, 14216 (2017). https://doi.org/10.1038/ncomms14216

57. Y.W. Li, Y.Y.Y. Xia, S.A. Ekahana, N. Kumar, J. Jiang et al., Topological origin of the type-II Dirac fermions in $PtSe_2$. Phys. Rev. Mater. **1**(7), 074202 (2017). https://doi.org/10.1103/PhysRevMaterials.1.074202

58. W. Zhang, J. Qin, Z. Huang, W. Zhang, The mechanism of layer number and strain dependent bandgap of 2D crystal $PtSe_2$. J. Appl. Phys. **122**, 205701 (2017). https://doi.org/10.1063/1.5000419

59. A. Jeremías Perea, B. Maria Andrea Andrea, A.M. Llois, Monolayer of $PtSe_2$ on Pt(111): is it metallic or insulating? J. Phys. Condens. Mater. **32**(23), 235002 (2020). https://doi.org/10.1088/1361-648X/ab73a5

60. Z. Hu, Z. Wu, C. Han, J. He, Z. Ni, W. Chen, Two-dimensional transition metal dichalcogenides: interface and defect engineering. Chem. Soc. Rev. **47**(9), 3100–3128 (2018). https://doi.org/10.1039/c8cs00024g

61. Q. Liu, L. Li, Y. Li, Z. Gao, Z. Chen, J. Lu, Tuning electronic structure of bilayer MoS_2 by vertical electric field: a first-principles investigation. J. Phys. Chem. C **116**(40), 21556–21562 (2012). https://doi.org/10.1021/jp307124d

62. S. Manzeli, A. Allain, A. Ghadimi, A. Kis, Piezoresistivity and strain-induced band gap tuning in atomically thin MoS_2. Nano Lett. **15**(8), 5330–5335 (2015). https://doi.org/10.1021/acs.nanolett.5b01689

63. Y. Liang, L. Yang, Carrier plasmon induced nonlinear band gap renormalization in two-dimensional semiconductors. Phys. Rev. Lett. **114**(6), 063001 (2015). https://doi.org/10.1103/PhysRevLett.114.063001

64. A. Bhattacharya, S. Bhattacharya, G.P. Das, Strain-induced band-gap deformation of H/F passivated graphene and h-BN sheet. Phys. Rev. B **84**(7), 075454 (2011). https://doi.org/10.1103/PhysRevB.84.075454

65. S. Deng, L. Li, Y. Zhang, Strain modulated electronic, mechanical, and optical properties of the monolayer PdS_2, $PdSe_2$, and $PtSe_2$ for tunable devices. ACS Appl. Nano Mater. **1**(4), 1932–1939 (2018). https://doi.org/10.1021/acsanm.8b00363

66. J. Du, P. Song, L. Fang, T. Wang, Z. Wei, J. Li, C. Xia, Elastic, electronic and optical properties of the two-dimensional PtX2 (X = S, Se, and Te) monolayer. Appl. Surf. Sci. **435**, 476–482 (2018). https://doi.org/10.1016/j.apsusc.2017.11.106

67. S.D. Guo, Biaxial strain tuned thermoelectric properties in monolayer $PtSe_2$. J. Mater. Chem. C **4**(39), 9366–9374 (2016). https://doi.org/10.1039/c6tc03074b

68. A. Kandemir, B. Akbali, Z. Kahraman, S.V. Badalov, M. Ozcan, F. Iyikanat, H. Sahin, Structural, electronic and phononic properties of $PtSe_2$: from monolayer to bulk. Semicond. Sci. Technol. **33**(8), 085002 (2018). https://doi.org/10.1088/1361-6641/aacba2

69. M. Kar, R. Sarkar, S. Pal, P. Sarkar, Engineering the magnetic properties of $PtSe_2$ monolayer through transition metal doping. J. Phys. Condens. Mater. **31**(14), 145502 (2019). https://doi.org/10.1088/1361-648X/aaff40

70. X. Lin, J.C. Lu, Y. Shao, Y.Y. Zhang, X. Wu et al., Intrinsically patterned two-dimensional materials for selective adsorption of molecules and nanoclusters. Nat. Mater. **16**(7), 717–721 (2017). https://doi.org/10.1038/nmat4915

71. H.-P. Komsa, S. Kurasch, O. Lehtinen, U. Kaiser, A.V.J.P.R.B. Krasheninnikov, From point to extended defects in two-dimensional MoS_2: evolution of atomic structure under electron irradiation. Phys. Rev. B **88**(3), 035301 (2013). https://doi.org/10.1103/PhysRevB.88.035301

72. Y.-C. Lin, D.O. Dumcenco, Y.-S. Huang, K.J.N.N. Suenaga, Atomic mechanism of the semiconducting-to-metallic phase transition in single-layered MoS_2. Nat. Nanotechnol. **9**(5), 391 (2014). https://doi.org/10.1038/nnano.2014.64

73. G.D. Nguyen, L. Liang, Q. Zou, M. Fu, A.D. Oyedele et al., 3D imaging and manipulation of subsurface selenium vacancies in $PdSe_2$. Phys. Rev. Lett. **121**(8), 086101 (2018). https://doi.org/10.1103/PhysRevLett.121.086101

74. J. Lin, S. Zuluaga, P. Yu, Z. Liu, S.T. Pantelides, K.J.P.R.L. Suenaga, Novel Pd_2Se_3 two-dimensional phase driven by interlayer fusion in layered $PdSe_2$. Phys. Rev. Lett. **119**(1), 016101 (2017). https://doi.org/10.1103/PhysRevLett.119.016101

75. G.H. Ryu, J. Chen, Y. Wen, J.H. Warner, In-situ atomic-scale dynamics of thermally driven phase transition of 2D few-layered 1T $PtSe_2$ into ultrathin 2D nonlayered PtSe crystals. Chem. Mater. **31**(23), 9895–9903 (2019). https://doi.org/10.1021/acs.chemmater.9b04274

76. Y. Yang, S.K. Jang, H. Choi, J. Xu, S. Lee, Homogeneous platinum diselenide metal/semiconductor coplanar structure fabricated by selective thickness control. Nanoscale **11**(44), 21068–21073 (2019). https://doi.org/10.1039/c9nr07995e

77. M.S. Shawkat, J. Gil, S.S. Han, T.-J. Ko, M. Wang et al., Thickness-independent semiconducting-to-metallic conversion in wafer-scale two-dimensional $PtSe_2$ layers by plasma-driven chalcogen defect engineering. ACS Appl. Mater. Interfaces **12**(12), 14341–14351 (2020). https://doi.org/10.1021/acsami.0c00116

78. M. O'Brien, N. McEvoy, C. Motta, J.Y. Zheng, N.C. Berner et al., Raman characterization of platinum diselenide thin films. 2D Mater. **3**(2), 021004 (2016). https://doi.org/10.1088/2053-1583/3/2/021004

79. C. Lee, H. Yan, L.E. Brus, T.F. Heinz, J. Hone, S.J.A.N. Ryu, Anomalous lattice vibrations of single-and few-layer MoS_2. ACS Nano **4**(5), 2695–2700 (2010). https://doi.org/10.1038/s41598-019-55755-x

80. H. Li, Q. Zhang, C.C.R. Yap, B.K. Tay, T.H.T. Edwin, A. Olivier, D.J.A.F.M. Baillargeat, From bulk to monolayer MoS_2: evolution of Raman scattering. Adv. Funct. Mater. **22**(7), 1385–1390 (2012). https://doi.org/10.1002/adfm.201102111

81. J. Xie, D. Zhang, X.-Q. Yan, M. Ren, X. Zhao et al., Optical properties of chemical vapor deposition-grown $PtSe_2$ characterized by spectroscopic ellipsometry. 2D Mater. **6**(3), 035011 (2019). https://doi.org/10.1088/2053-1583/ab1490

82. X. Zhao, F. Liu, D.Q. Liu, X.Q. Yan, C.F. Huo et al., Thickness-dependent ultrafast nonlinear absorption properties of $PtSe_2$ films with both semiconducting and semimetallic phases. Appl. Phys. Lett. **115**(26), 263102 (2019). https://doi.org/10.1063/1.5135375

83. X. Chen, S.F. Zhang, L. Wang, Y.F. Huang, H.N. Liu et al., Direct observation of interlayer coherent acoustic phonon dynamics in bilayer and few-layer $PtSe_2$. Photonics Res. **7**(12), 1416–1424 (2019). https://doi.org/10.1364/prj.7.001416

84. L. Wang, S.F. Zhang, N. McEvoy, Y.Y. Sun, J.W. Huang et al., Nonlinear optical signatures of the transition from semiconductor to semimetal in $PtSe_2$. Laser Photonics Rev. **13**(8), 1900052 (2019). https://doi.org/10.1002/lpor.201900052

85. Y. Ge, Z. Zhu, Y. Xu, Y. Chen, S. Chen et al., Broadband nonlinear photoresponse of 2D TiS_2 for ultrashort pulse generation and all-optical thresholding devices. Adv. Opt. Mater. **6**(4), 1701166 (2018). https://doi.org/10.1002/adom.201701166

86. B. Guo, S.-H. Wang, Z.-X. Wu, Z.-X. Wang, D.-H. Wang et al., Sub-200 fs soliton mode-locked fiber laser based on bismuthene saturable absorber. Opt. Exp. **26**(18), 22750 (2018). https://doi.org/10.1364/oe.26.022750

87. X. Jiang, S. Liu, W. Liang, S. Luo, Z. He et al., Broadband nonlinear photonics in few-layer MXene $Ti_3C_2T_x$ (T = F, O, or OH). Laser Photonics Rev. **12**(2), 1700229–1700239 (2018). https://doi.org/10.1002/lpor.201700229

88. X. Jiang, L. Zhang, S. Liu, Y. Zhang, Z. He et al., Ultrathin metal-organic framework: an emerging broadband nonlinear optical material for ultrafast photonics. Adv. Opt. Mater. **6**(16), 1800561 (2018). https://doi.org/10.1002/adom.201800561

89. M. Zhang, Q. Wu, F. Zhang, L. Chen, X. Jin et al., 2D Black phosphorus saturable absorbers for ultrafast photonics. Adv. Opt. Mater. **7**(1), 1800224 (2018). https://doi.org/10.1002/adom.201800224

90. C. Ma, C. Wang, B. Gao, J. Adams, G. Wu, H. Zhang, Recent progress in ultrafast lasers based on 2D materials as a saturable absorber. Appl. Phys. Rev. **6**(4), 041304 (2019). https://doi.org/10.1063/1.5099188

91. T. Jiang, K. Yin, C. Wang, J. You, H. Ouyang et al., Ultrafast fiber lasers mode-locked by two-dimensional materials: review and prospect. Photonics Res. **8**(1), 78 (2019). https://doi.org/10.1364/prj.8.000078

92. Y. Song, X. Shi, C. Wu, D. Tang, H. Zhang, Recent progress of study on optical solitons in fiber lasers. Appl. Phys. Rev. **6**(2), 021313 (2019). https://doi.org/10.1063/1.5091811

93. Y. Fang, Y. Ge, C. Wang, H. Zhang, Mid-infrared photonics using 2D materials: status and challenges. Laser Photonics Rev. **14**(1), 1900098 (2019). https://doi.org/10.1002/lpor.201900098

94. L.L. Tao, X.W. Huang, J.S. He, Y.J. Lou, L.H. Zeng et al., Vertically standing PtSe$_2$ film: a saturable absorber for a passively mode-locked Nd:LuVO$_4$ laser. Photonics Res. **6**(7), 750–755 (2018). https://doi.org/10.1364/Prj.6.000750

95. K. Zhang, M. Feng, Y.Y. Ren, F. Liu, X.S. Chen et al., Q-switched and mode-locked Er-doped fiber laser using PtSe$_2$ as a saturable absorber. Photonics Res. **6**(9), 893–899 (2018). https://doi.org/10.1364/Prj.6.000893

96. J. Guo, J. Zhao, D. Huang, Y. Wang, F. Zhang et al., Two-dimensional tellurium-polymer membrane for ultrafast photonics. Nanoscale **11**(13), 6235–6242 (2019). https://doi.org/10.1039/c9nr00736a

97. L. Lu, Z. Liang, L. Wu, Y. Chen, Y. Song et al., Few-layer bismuthene: sonochemical exfoliation, nonlinear optics and applications for ultrafast photonics with enhanced stability. Laser Photonics Rev. **12**(1), 1700221 (2018). https://doi.org/10.1002/lpor.201700221

98. W. Tao, X. Zhu, X. Yu, X. Zeng, Q. Xiao et al., Black phosphorus nanosheets as a robust delivery platform for cancer theranostics. Adv. Mater. **29**(1), 1603276 (2017). https://doi.org/10.1002/adma.201603276

99. S. Park, R.S. Ruoff, Chemical methods for the production of graphenes. Nat. Nanotechnol. **4**(4), 217–224 (2009). https://doi.org/10.1038/nnano.2009.58

100. B. Huang, L. Du, Q. Yi, L.L. Yang, J. Li et al., Bulk-structured PtSe$_2$ for femtosecond fiber laser mode-locking. Opt. Exp. **27**(3), 2604–2611 (2019). https://doi.org/10.1364/oe.27.002604

101. J. Sun, C. Lu, Y. Song, Q. Ji, X. Song et al., Recent progress in the tailored growth of two-dimensional hexagonal boron nitride via chemical vapour deposition. Chem. Soc. Rev. **47**(12), 4242–4257 (2018). https://doi.org/10.1039/c8cs00167g

102. J. Wang, Z. Li, H. Chen, G. Deng, X. Niu, Recent advances in 2D lateral heterostructures. Nano-Micro Lett. **11**(1), 45 (2019). https://doi.org/10.1007/s40820-019-0276-y

103. C. Yang, M. Zhou, C. He, Y. Gao, S. Li et al., Augmenting intrinsic fenton-like activities of MOF-derived catalysts via n-molecule-assisted self-catalyzed carbonization. Nano-Micro Lett. **11**(1), 87 (2019). https://doi.org/10.1007/s40820-019-0319-4

104. H. Xu, J. Zhu, G. Zou, W. Liu, X. Li et al., Spatially bandgap-graded MoS$_{2(1-x)}$Se$_{2x}$ homojunctions for self-powered visible-near-infrared phototransistors. Nano-Micro Lett. **12**(1), 26 (2020). https://doi.org/10.1007/s40820-019-0361-2

105. W.J. Wang, K.L. Li, Y. Wang, W.X. Jiang, X.Y. Liu, H. Qi, Investigation of the band alignment at MoS$_2$/PtSe$_2$ heterojunctions. Appl. Phys. Lett. **114**(20), 201601 (2019). https://doi.org/10.1063/1.5097248

106. Z.G. Wang, Q. Li, F. Besenbacher, M.D. Dong, Facile synthesis of single crystal PtSe$_2$ nanosheets for nanoscale electronics. Adv. Mater. **28**(46), 10224–10229 (2016). https://doi.org/10.1002/adma.201602889

107. H. Xu, H.M. Zhang, Y.W. Liu, S.M. Zhang, Y.Y. Sun et al., Controlled doping of wafer-scale PtSe$_2$ films for device application. Adv. Funct. Mater. **29**(4), 1805614 (2019). https://doi.org/10.1002/adfm.201805614

108. B. Yan, B. Zhang, H. Nie, G. Li, J. Liu, B. Shi, K. Yang, J. He, Bilayer platinum diselenide saturable absorber for 2.0 mum passively Q-switched bulk lasers. Opt Exp. **26**(24), 31657–31663 (2018). https://doi.org/10.1364/OE.26.031657

109. R. Gatensby, N. McEvoy, K. Lee, T. Hallam, N.C. Berner et al., Controlled synthesis of transition metal dichalcogenide thin films for electronic applications. Appl. Surf. Sci. **297**, 139–146 (2014). https://doi.org/10.1016/j.apsusc.2014.01.103

110. R. Gatensby, T. Hallam, K. Lee, N. McEvoy, G.S.J.S.-S.E. Duesberg, Investigations of vapour-phase deposited transition metal dichalcogenide films for future electronic applications. Solid State Electron. **125**, 39–51 (2016). https://doi.org/10.1016/j.sse.2016.07.021

111. J.B. Mc Manus, G. Cunningham, N. McEvoy, C.P. Cullen, F. Gity et al., Growth of 1T' MoTe$_2$ by thermally assisted conversion of electrodeposited tellurium films. ACS Appl. Energy Mater. **2**(1), 521–530 (2019). https://doi.org/10.1021/acsaem.8b01540

112. C. Yim, K. Lee, N. McEvoy, M. O'Brien, S. Riazimehr et al., High-performance hybrid electronic devices from layered PtSe$_2$ films grown at low temperature. ACS Nano **10**(10), 9550–9558 (2016). https://doi.org/10.1021/acsnano.6b04898

113. C. Yim, V. Passi, M.C. Lemme, G.S. Duesberg, C.O. Coileain et al., Electrical devices from top-down structured platinum diselenide films. NPJ 2D Mater. Appl. **2**, 5 (2018). https://doi.org/10.1038/s41699-018-0051-9

114. S.S. Han, J.H. Kim, C. Noh, J.H. Kim, E. Ji et al., Horizontal-to-vertical transition of 2D layer orientation in low-temperature chemical vapor deposition-grown PtSe$_2$ and its influences on electrical properties and device applications. ACS Appl. Mater. Interfaces **11**(14), 13598–13607 (2019). https://doi.org/10.1021/acsami.9b01078

115. M.S. Shawkat, H.S. Chung, D. Dev, S. Das, T. Roy, Y. Jung, Two-dimensional/three-dimensional schottky junction photovoltaic devices realized by the direct CVD growth of vdW 2D PtSe$_2$ layers on silicon. ACS Appl. Mater. Interfaces **11**(30), 27251–27258 (2019). https://doi.org/10.1021/acsami.9b09000

116. C. Xie, L.H. Zeng, Z.X. Zhang, Y.H. Tsang, L.B. Luo, J.H. Lee, High-performance broadband heterojunction photodetectors based on multilayered PtSe$_2$ directly grown on a Si substrate. Nanoscale **10**(32), 15285–15293 (2018). https://doi.org/10.1039/c8nr04004d

117. J. Yuan, T. Sun, Z.X. Hu, W.Z. Yu, W.L. Ma et al., Wafer-scale fabrication of two-dimensional PtS$_2$/PtSe$_2$ heterojunctions for efficient and broad band photodetection. ACS Appl. Mater. Interfaces **10**(47), 40614–40622 (2018). https://doi.org/10.1021/acsami.8b13620

118. L. Wang, J.-J. Li, Q. Fan, Z.-F. Huang, Y.-C. Lu et al., A high-performance near-infrared light photovoltaic detector based on a multilayered PtSe$_2$/Ge heterojunction. J. Mater. Chem. C **7**(17), 5019–5027 (2019). https://doi.org/10.1039/c9tc00797k

119. L. Ansari, S. Monaghan, N. McEvoy, C.O. Coileain, C.P. Cullen et al., Quantum confinement-induced semimetal-to-semiconductor evolution in large-area ultra-thin PtSe2 films grown at 400 °C. NPJ 2D Mater. Appl. **3**, 33 (2019). https://doi.org/10.1038/s41699-019-0116-4

120. L.H. Zeng, S.H. Lin, Z.J. Li, Z.X. Zhang, T.F. Zhang et al., Fast, self-driven, air-stable, and broadband photodetector based on vertically aligned PtSe$_2$/GaAs heterojunction. Adv. Funct. Mater. **28**(16), 1705970 (2018). https://doi.org/10.1002/adfm.201705970

121. D. Wu, Y.E. Wang, L.H. Zeng, C. Jia, E.P. Wu et al., Design of 2D layered PtSe$_2$ heterojunction for the high-performance, room-temperature, broadband, infrared photodetector. ACS Photonics **5**(9), 3820–3827 (2018). https://doi.org/10.1021/acsphotonics.8b00853

122. S. Wagner, C. Yim, N. McEvoy, S. Kataria, V. Yokaribas et al., Highly sensitive electromechanical piezoresistive pressure sensors based on large-area layered PtSe$_2$ films. Nano Lett. **18**(6), 3738–3745 (2018). https://doi.org/10.1021/acs.nanolett.8b00928

123. Z.X. Zhang, Z. Long-Hui, X.W. Tong, Y. Gao, C. Xie et al., self-driven, and air-stable photodetectors based on multilayer PtSe$_2$/perovskite heterojunctions. J. Phys. Chem. Lett. **9**(6), 1185–1194 (2018). https://doi.org/10.1021/acs.jpclett.8b00266

124. L. Li, K.C. Xiong, R.J. Marstell, A. Madjar, N.C. Strandwitz et al., Wafer-scale fabrication of recessed-channel PtSe$_2$ MOSFETs with low contact resistance and improved gate control. IEEE Trans. Electron Dev. **65**(10), 4102–4108 (2018). https://doi.org/10.1109/Ted.2018.2856305

125. J. He, Y. Li, Y. Lou, G. Zeng, L. Tao, Optical deposition of PtSe$_2$ on fiber end face for Yb-doped mode-locked fiber laser. Optik **198**, 163298 (2019). https://doi.org/10.1016/j.ijleo.2019.163298

126. Z.Q. Li, R. Li, C. Pang, N.N. Dong, J. Wang, H.H. Yu, F. Chen, 8.8 GHz Q-switched mode-locked waveguide lasers modulated by PtSe$_2$ saturable absorber. Opt. Exp. **27**(6), 8727–8737 (2019). https://doi.org/10.1364/oe.27.008727

127. X.N. Sun, H.C. Zhang, X.T. Li, Y.Z. Zheng, J.J. Wu et al., An efficient and extremely stable photocatalytic PtSe$_2$/FTO thin film for water splitting. Energy Technol. **8**(1), 1900903 (2020). https://doi.org/10.1002/ente.201900903

128. S. Lin, Y. Liu, Z. Hu, W. Lu, C.H. Mak et al., Tunable active edge sites in PtSe$_2$ films towards hydrogen evolution reaction. Nano Energy **42**, 26–33 (2017). https://doi.org/10.1016/j.nanoen.2017.10.038

129. R.R. Zhuo, L.H. Zeng, H.Y. Yuan, D. Wu, Y.G. Wang et al., In-situ fabrication of PtSe$_2$/GaN heterojunction for self-powered deep ultraviolet photodetector with ultrahigh current on/off ratio and detectivity. Nano Res. **12**(1), 183–189 (2019). https://doi.org/10.1007/s12274-018-2200-z

130. K. Ullah, S. Ye, S.S. Jo, L. Zhu, K.Y. Cho, W.C. Oh, Optical and photocatalytic properties of novel heterogeneous PtSe$_2$-graphene/TiO$_2$ nanocomposites synthesized via ultrasonic assisted techniques. Ultrason. Sonochem. **21**(5), 1849–1857 (2014). https://doi.org/10.1016/j.ultsonch.2014.04.016

131. K. Ullah, L. Zhu, Z.-D. Meng, S. Ye, S. Sarkar, W.-C. Oh, Synthesis and characterization of novel PtSe$_2$/graphene nanocomposites and its visible light driven catalytic properties. J. Mater. Sci. **49**(12), 4139–4147 (2014). https://doi.org/10.1007/s10853-014-8109-3

132. K. Ullah, S. Ye, Z. Lei, K.Y. Cho, W.C. Oh, Synergistic effect of PtSe$_2$ and graphene sheets supported by TiO$_2$ as cocatalysts synthesized via microwave techniques for improved photocatalytic activity. Catal. Sci. Technol. **5**(1), 184–198 (2015). https://doi.org/10.1039/c4cy00886c

133. S. Ye, W.C. Oh, Demonstration of enhanced the photocatalytic effect with PtSe$_2$ and TiO$_2$ treated large area graphene obtained by CVD method. Mater. Sci. Semicond. Proc. **48**, 106–114 (2016). https://doi.org/10.1016/j.mssp.2016.03.001

134. K. Ullah, S.B. Jo, S. Ye, L. Zhu, W.C. Oh, Visible light driven catalytic properties over methyl orange by novel PtSe$_2$/graphene nanocomposites. Asian J. Chem. **26**(6), 1575–1579 (2014). https://doi.org/10.14233/ajchem.2014.17292

135. A.A. Umar, S.K.M. Saad, M.M. Salleh, Scalable mesoporous platinum diselenide nanosheet synthesis in water. ACS Omega **2**(7), 3325–3332 (2017). https://doi.org/10.1021/acsomega.7b00580

136. M.S. Pawar, D.J. Late, Temperature-dependent Raman spectroscopy and sensor applications of PtSe$_2$ nanosheets synthesized by wet chemistry. Beilstein J. Nanotechnol. **10**, 467–474 (2019). https://doi.org/10.3762/bjnano.10.46

137. K. Klosse, P. Ullersma, Convection in a chemical vapor transport process. J. Cryst. Growth **18**(2), 167–174 (1973). https://doi.org/10.1016/0022-0248(73)90195-4

138. D. Hu, G. Xu, L. Xing, X. Yan, J. Wang et al., Two-dimensional semiconductors grown by chemical vapor transport. Angew. Chem. Int. Ed. **56**(13), 3611–3615 (2017). https://doi.org/10.1002/anie.201700439

139. J. Wang, H. Zheng, G. Xu, L. Sun, D. Hu et al., Controlled synthesis of two-dimensional 1T-TiSe$_2$ with charge density wave transition by chemical vapor transport. J. Am. Chem. Soc. **138**(50), 16216–16219 (2016). https://doi.org/10.1021/jacs.6b10414

140. Z. Du, C. Zhang, M. Wang, X. Zhang, J. Ning et al., Synthesis of WS$_{1.76}$Te$_{0.24}$ alloy through chemical vapor transport and its high-performance saturable absorption. Sci. Rep. **9**(1), 1–9 (2019). https://doi.org/10.1038/s41598-019-55755-x

141. Y. Zhao, S.J.A.M.L. Jin, Controllable water vapor assisted chemical vapor transport synthesis of WS$_2$MoS$_2$ heterostructure. ACS Mater. Lett. **2**(1), 42–48 (2019). https://doi.org/10.1103/PhysRevLett.121.086101

142. D. Hu, T. Zhao, X. Ping, H. Zheng, L. Xing et al., Unveiling the layer-dependent catalytic activity of $PtSe_2$ atomic crystals for the hydrogen evolution reaction. Angew. Chem. Int. Ed. **58**(21), 6977–6981 (2019). https://doi.org/10.1002/anie.201901612

143. C.-F. Du, Q. Liang, R. Dangol, J. Zhao, H. Ren, S. Madhavi, Q. Yan, Layered trichalcogenidophosphate: a new catalyst family for water splitting. Nano-Micro Lett. **10**(4), 67 (2018). https://doi.org/10.1007/s40820-018-0220-6

144. Z. Zhang, D.-H. Xing, J. Li, Q. Yan, Hittorf's phosphorus: the missing link during transformation of red phosphorus to black phosphorus. CrystEngComm **19**(6), 905–909 (2017). https://doi.org/10.1039/c6ce02550a

145. H.-A. Chen, H. Sun, C.-R. Wu, Y.-X. Wang, P.-H. Lee, C.-W. Pao, S.-Y. Lin, Single-crystal antimonene films prepared by molecular beam epitaxy: selective growth and contact resistance reduction of the 2D material heterostructure. ACS Appl. Mater. Interfaces **10**(17), 15058–15064 (2018). https://doi.org/10.1021/acsami.8b02394

146. H.C. Diaz, Y. Ma, R. Chaghi, M. Batzill, High density of (pseudo) periodic twin-grain boundaries in molecular beam epitaxy-grown van der Waals heterostructure: $MoTe_2$/MoS_2. Appl. Phys. Lett. **108**(19), 191606 (2016). https://doi.org/10.1063/1.4949559

147. X. Fan, L. Su, F. Zhang, D. Huang, D.K. Sang et al., Layer-dependent properties of ultrathin GeS nanosheets and application in UV–Vis photodetectors. ACS Appl. Mater. Interfaces **11**(50), 47197–47206 (2019). https://doi.org/10.1021/acsami.9b14663

148. D. Tyagi, H. Wang, W. Huang, L. Hu, Y. Tang et al., Recent advances in two-dimensional-material-based sensing technology toward health and environmental monitoring applications. Nanoscale **12**(6), 3535–3559 (2020). https://doi.org/10.1039/c9nr10178k

149. D. Ma, R. Wang, J. Zhao, Q. Chen, L. Wu et al., A self-powered photodetector based on two-dimensional boron nanosheets. Nanoscale **12**(9), 5313–5323 (2020). https://doi.org/10.1039/d0nr00005a

150. Y. Yin, R. Cao, J. Guo, C. Liu, J. Li et al., High-speed and high-responsivity hybrid silicon/black-phosphorus waveguide photodetectors at 2 μm. Laser Photonics Rev. **13**(6), 1900032 (2019). https://doi.org/10.1002/lpor.201900032

151. R. Cao, H.-D. Wang, Z.-N. Guo, D.K. Sang, L.-Y. Zhang et al., Black phosphorous/indium selenide photoconductive detector for visible and near-infrared light with high sensitivity. Adv. Opt. Mater. **7**(12), 1900020 (2019). https://doi.org/10.1002/adom.201900020

152. Y. Ding, N. Zhou, L. Gan, X.X. Yan, R.Z. Wu et al., Stacking-mode confined growth of $2H-MoTe_2$/MoS_2 bilayer heterostructures for UV-vis-IR photodetectors. Nano Energy **49**, 200–208 (2018). https://doi.org/10.1016/j.nanoen.2018.04.055

153. N. Huo, G. Konstantatos, Recent progress and future prospects of 2D-based photodetectors. Adv. Mater. **30**(51), e1801164 (2018). https://doi.org/10.1002/adma.201801164

154. Y. Ma, Ultrathin $SnSe_2$ flakes: a new member in two-dimensional materials for high-performance photodetector. Sci. Bull. **60**(20), 1789–1790 (2015). https://doi.org/10.1007/s11434-015-0907-8

155. Y. Zhang, F. Zhang, Y. Xu, W. Huang, L. Wu et al., Self-healable black phosphorus photodetectors. Adv. Funct. Mater. **29**(49), 1906610 (2019). https://doi.org/10.1002/adfm.201906610

156. E. Wu, D. Wu, C. Jia, Y. Wang, H. Yuan et al., In situ fabrication of 2D WS_2/Si type-ii heterojunction for self-powered broadband photodetector with response up to mid-infrared. ACS Photonics **6**(2), 565 (2019). https://doi.org/10.1021/acsphotonics.8b01675

157. C. Jia, X. Huang, D. Wu, Y. Tian, J. Guo et al., An ultrasensitive self-driven broadband photodetector based on a 2D-WS_2/GaAs type-II Zener heterojunction. Nanoscale **12**(7), 4435–4444 (2020). https://doi.org/10.1039/c9nr10348a

158. Z. Lou, L. Zeng, Y. Wang, D. Wu, T. Xu et al., High-performance MoS_2/Si heterojunction broadband photodetectors from deep ultraviolet to near infrared. Opt. Lett. **42**(17), 3335–3338 (2017). https://doi.org/10.1364/ol.42.003335

159. L.-H. Zeng, D. Wu, S.-H. Lin, C. Xie, H.-Y. Yuan et al., Controlled synthesis of 2D Palladium diselenide for sensitive photodetector applications. Adv. Funct. Mater. **29**(1), 1806878 (2019). https://doi.org/10.1002/adfm.201806878

160. L.H. Zeng, S.H. Lin, Z.H. Lou, H.Y. Yuan, H. Long et al., Ultrafast and sensitive photodetector based on a $PtSe_2$/silicon nanowire array heterojunction with a multiband spectral response from 200 to 1550 nm. NPG Asia Mater. **10**, 352–362 (2018). https://doi.org/10.1038/s41427-018-0035-4

161. Y.H. Zhou, Z.B. Zhang, P. Xu, H. Zhang, B. Wang, UV-visible photodetector based on i-type heterostructure of ZnO-QDs/monolayer MoS_2. Nanoscale Res. Lett. **14**(1), 364 (2019). https://doi.org/10.1186/s11671-019-3183-8

162. K. Chen, Y. Wang, J. Liu, J. Kang, Y. Ge et al., In situ preparation of a $CsPbBr_3$/black phosphorus heterostructure with an optimized interface and photodetector application. Nanoscale **11**(36), 16852–16859 (2019). https://doi.org/10.1039/c9nr06488e

163. D. Ma, J. Zhao, R. Wang, C. Xing, Z. Li et al., Ultrathin GeSe nanosheets: from systematic synthesis to studies of carrier dynamics and applications for a high-performance UV–Vis photodetector. ACS Appl. Mater. Interfaces **11**(4), 4278–4287 (2019). https://doi.org/10.1021/acsami.8b19836

164. Y. Chen, X. Wu, Y. Chu, J. Zhou, B. Zhou, J. Huang, Hybrid field-effect transistors and photodetectors based on organic semiconductor and $CsPbI_3$ perovskite nanorods bilayer structure. Nano-Micro Lett. **10**(4), 57 (2018). https://doi.org/10.1007/s40820-018-0210-8

165. C. Jung, S.M. Kim, H. Moon, G. Han, J. Kwon et al., Highly crystalline CVD-grown multilayer $MoSe_2$ thin film transistor for fast photodetector. Sci. Rep. **5**, 15313 (2015). https://doi.org/10.1038/srep15313

166. J. Xia, X. Huang, L.-Z. Liu, M. Wang, L. Wang et al., CVD synthesis of large-area, highly crystalline $MoSe_2$ atomic layers on diverse substrates and application to

photodetectors. Nanoscale **6**(15), 8949–8955 (2014). https://doi.org/10.1039/c4nr02311k

167. S. Yang, C. Wang, C. Ataca, Y. Li, H. Chen et al., Self-driven photodetector and ambipolar transistor in atomically thin GaTe–MoS₂ p–n vdW heterostructure. ACS Appl. Mater. Interfaces **8**(4), 2533–2539 (2016). https://doi.org/10.1021/acsami.5b10001

168. L.-B. Luo, H. Hu, X.-H. Wang, R. Lu, Y.-F. Zou, Y.-Q. Yu, F.-X. Liang, A graphene/GaAs near-infrared photodetector enabled by interfacial passivation with fast response and high sensitivity. J. Mater. Chem. C **3**(18), 4723–4728 (2015). https://doi.org/10.1039/c5tc00449g

169. M. Buscema, D.J. Groenendijk, S.I. Blanter, G.A. Steele, H.S.J. van der Zant, A. Castellanos-Gomez, Fast and broadband photoresponse of few-layer black phosphorus field-effect transistors. Nano Lett. **14**(6), 3347–3352 (2014). https://doi.org/10.1021/nl5008085

170. W. Choi, M.Y. Cho, A. Konar, J.H. Lee, G.-B. Cha et al., High-detectivity multilayer MoS₂ phototransistors with spectral response from ultraviolet to infrared. Adv. Mater. **24**(43), 5832–5836 (2012). https://doi.org/10.1002/adma.201201909

171. X. Chen, J.S. Ponraj, D. Fan, H. Zhang, An overview of the optical properties and applications of black phosphorus. Nanoscale **12**(6), 3513–3534 (2020). https://doi.org/10.1039/c9nr09122j

172. Q. Zhang, X. Jiang, M. Zhang, X. Jin, H. Zhang, Z. Zheng, Wideband saturable absorption in metal-organic frameworks (MOFs) for mode-locking Er- and Tm-doped fiber lasers. Nanoscale **12**(7), 4586–4590 (2020). https://doi.org/10.1039/c9nr09330c

173. B. Lomsadze, K.M. Fradet, R.S. Arnold, Elastic tape behavior of a bi-directional Kerr-lens mode-locked dual-comb ring laser. Opt. Lett. **45**(5), 1080–1083 (2020). https://doi.org/10.1364/ol.386160

174. L. Li, L. Zhou, T. Li, X. Yang, W. Xie et al., Passive mode-locking operation of a diode-pumped Tm:YAG laser with a MoS₂ saturable absorber. Opt. Laser Technol. **124**, 355–359 (2020). https://doi.org/10.1016/j.optlastec.2019.105986

175. Z. Sun, T. Hasan, F. Torrisi, D. Popa, G. Privitera, F. Wang, F. Bonaccorso, D.M. Basko, A.C. Ferrari, Graphene mode-locked ultrafast laser. ACS Nano **4**(2), 803–810 (2010). https://doi.org/10.1021/nn901703e

176. D.J. Jones, S.A. Diddams, J.K. Ranka, A. Stentz, R.S. Windeler, J.L. Hall, S.T. Cundiff, Carrier-envelope phase control of femtosecond mode-locked lasers and direct optical frequency synthesis. Science **288**(5466), 635–639 (2000). https://doi.org/10.1126/science.288.5466.635

177. J. Yuan, H. Mu, L. Li, Y. Chen, W. Yu et al., Few-layer platinum diselenide as a new saturable absorber for ultrafast fiber lasers. ACS Appl. Mater. Interfaces **10**(25), 21534–21540 (2018). https://doi.org/10.1021/acsami.8b03045

178. W. Zhang, Z. Huang, W. Zhang, Y. Li, Two-dimensional semiconductors with possible high room temperature mobility. Nano Res. **7**(12), 1731–1737 (2014). https://doi.org/10.1007/s12274-014-0532-x

179. S.-L. Li, K. Wakabayashi, Y. Xu, S. Nakaharai, K. Komatsu et al., Thickness-dependent interfacial coulomb scattering in atomically thin field-effect transistors. Nano Lett. **13**(8), 3546–3552 (2013). https://doi.org/10.1021/nl4010783

180. E. Okogbue, S.S. Han, T.J. Ko, H.S. Chung, J. Ma et al., Multifunctional two-dimensional PtSe₂-layer kirigami conductors with 2000% stretchability and metallic-to-semiconducting tunability. Nano Lett. **19**(11), 7598–7607 (2019). https://doi.org/10.1021/acs.nanolett.9b01726

181. S. Kim, A. Konar, W.-S. Hwang, J.H. Lee, J. Lee et al., High-mobility and low-power thin-film transistors based on multilayer MoS₂ crystals. Nat. Commun. **3**(1), 1011 (2012). https://doi.org/10.1038/ncomms2018

182. Z. Yu, Y. Pan, Y. Shen, Z. Wang, Z.-Y. Ong et al., Towards intrinsic charge transport in monolayer molybdenum disulfide by defect and interface engineering. Nat. Commun. **5**(1), 5290 (2014). https://doi.org/10.1038/ncomms6290

183. Z. Yu, Z.-Y. Ong, Y. Pan, Y. Cui, R. Xin et al., Realization of room-temperature phonon-limited carrier transport in monolayer MoS₂ by dielectric and carrier screening. Adv. Mater. **28**(3), 547–552 (2016). https://doi.org/10.1002/adma.201503033

184. H. Wang, D.K. Sang, Z. Guo, R. Cao, J. Zhao et al., Black phosphorus-based field effect transistor devices for Ag ions detection. Chin. Phys. B **27**(8), 087308 (2018). https://doi.org/10.1088/1674-1056/27/8/087308

185. J. Zhang, Y. Chen, X. Wang, Two-dimensional covalent carbon nitride nanosheets: synthesis, functionalization, and applications. Energy Environ. Sci. **8**(11), 3092–3108 (2015). https://doi.org/10.1039/c5ee01895a

186. Q. Lu, Y. Yu, Q. Ma, B. Chen, H. Zhang, 2D transition-metal-dichalcogenide-nanosheet-based composites for photocatalytic and electrocatalytic hydrogen evolution reactions. Adv. Mater. **28**(10), 1917–1933 (2016). https://doi.org/10.1002/adma.201503270

187. D. Li, W. Wu, Y. Zhang, L. Liu, C. Pan, Preparation of ZnO/graphene heterojunction via high temperature and its photocatalytic property. J. Mater. Sci. **49**(4), 1854–1860 (2014). https://doi.org/10.1007/s10853-013-7873-9

188. Y.P. Zhang, C.X. Pan, TiO₂/graphene oxide and its photocatalytic activity in visible light. J. Mater. Sci. **46**(8), 2622–2626 (2011). https://doi.org/10.1007/s10853-010-5116-x

189. R. Asahi, T. Morikawa, T. Ohwaki, K. Aoki, Y.J.S. Taga, Visible-light photocatalysis in nitrogen-doped titanium oxides. Science **293**(5528), 269–271 (2001). https://doi.org/10.1126/science.1061051

190. Y.X. Chen, K.N. Yang, B. Jiang, J.X. Li, M.Q. Zeng, L. Fu, Emerging two-dimensional nanomaterials for electrochemical hydrogen evolution. J. Mater. Chem. A **5**(18), 8187–8208 (2017). https://doi.org/10.1039/c7ta00816c

191. B. Jo'M, The origin of ideas on a hydrogen economy and its solution to the decay of the environment. Int. J. Hydrogen Energy **27**(7–8), 731–740 (2002). https://doi.org/10.1016/S0360-3199(01)00154-9

192. B. Ma, T.-T. Chen, Q.-Y. Li, H.-N. Qin, X.-Y. Dong, S.-Q. Zang, Bimetal-organic-framework-derived nanohybrids

$Cu_{0.9}Co_{2.1}S_4$@MoS_2 for high-performance visible-light-catalytic hydrogen evolution reaction. ACS Appl. Energy Mater. **2**(2), 1134–1148 (2019). https://doi.org/10.1021/acsaem.8b01691

193. S.R. Kadam, U.V. Kawade, R. Bar-Ziv, S.W. Gosavi, M. Bar-Sadan, B.B. Kale, Porous MoS_2 framework and its functionality for electrochemical hydrogen evolution reaction and lithium ion batteries. ACS Appl. Energy Mater. **2**(8), 5900–5908 (2019). https://doi.org/10.1021/acsaem.9b01045

194. H. Wang, Z. Lu, D. Kong, J. Sun, T.M. Hymel, Y. Cui, Electrochemical tuning of MoS_2 nanoparticles on three-dimensional substrate for efficient hydrogen evolution. ACS Nano **8**(5), 4940–4947 (2014). https://doi.org/10.1021/nn500959v

195. H. Wang, Z. Lu, S. Xu, D. Kong, J.J. Cha et al., Electrochemical tuning of vertically aligned MoS_2 nanofilms and its application in improving hydrogen evolution reaction. Proc. Natl. Acad. Sci. USA **110**(49), 19701–19706 (2013). https://doi.org/10.1073/pnas.1316792110

196. X. Chia, A. Adriano, P. Lazar, Z. Sofer, J. Luxa, M. Pumera, Layered platinum dichalcogenides (PtS_2, $PtSe_2$, and $PtTe_2$) electrocatalysis: monotonic dependence on the chalcogen size. Adv. Funct. Mater. **26**(24), 4306–4318 (2016). https://doi.org/10.1002/adfm.201505402

197. J. Shi, Y. Huan, M. Hong, R. Xu, P. Yang et al., Chemical vapor deposition grown large-scale atomically thin platinum diselenide with semimetal-semiconductor transition. ACS Nano **13**(7), 8442–8451 (2019). https://doi.org/10.1021/acsnano.9b04312

198. H. Huang, X. Fan, D.J. Singh, W. Zheng, Modulation of hydrogen evolution catalytic activity of basal plane in monolayer platinum and palladium dichalcogenides. ACS Omega **3**(8), 10058–10065 (2018). https://doi.org/10.1021/acsomega.8b01414

199. M. Sajjad, E. Montes, N. Singh, U. Schwingenschlogl, Superior gas sensing properties of monolayer $PtSe_2$. Adv. Mater. Inter. **4**(5), 1600911 (2017). https://doi.org/10.1002/admi.201600911

200. D.C. Chen, X.X. Zhang, J. Tang, Z.L. Cui, H. Cui, S.M. Pi, Theoretical study of monolayer $PtSe_2$ as outstanding gas sensor to detect SF6 decompositions. IEEE Electr. Device Lett. **39**(9), 1405–1408 (2018). https://doi.org/10.1109/Led.2018.2859258

201. J. Zhang, G. Yang, J. Tian, D. Ma, Y. Wang, First-principles study on the gas sensing property of the Ge, As, and Br doped $PtSe_2$. Mater. Res. Exp. **5**(3), 05037 (2018). https://doi.org/10.1088/2053-1591/aab4e3

202. M.G. Chung, D.H. Kim, H.M. Lee, T. Kim, J.H. Choi et al., Highly sensitive NO2 gas sensor based on ozone treated graphene. Sensor. Actuat. B **166**, 172–176 (2012). https://doi.org/10.1016/j.snb.2012.02.036

203. B. Liu, L. Chen, G. Liu, A.N. Abbas, M. Fathi, C. Zhou, High-performance chemical sensing using Schottky-contacted chemical vapor deposition grown mono layer MoS_2 transistors. ACS Nano **8**(5), 5304–5314 (2014). https://doi.org/10.1021/nn5015215

204. B. Cho, A.R. Kim, Y. Park, J. Yoon, Y.-J. Lee et al., Bifunctional sensing characteristics of chemical vapor deposition synthesized atomic-layered MoS_2. ACS Appl. Mater. Interfaces **7**(4), 2952–2959 (2015). https://doi.org/10.1021/am508535x

205. Y.H. Kim, S.J. Kim, Y.-J. Kim, Y.-S. Shim, S.Y. Kim, B.H. Hong, H.W. Jang, Self-activated transparent all-graphene gas sensor with endurance to humidity and mechanical bending. ACS Nano **9**(10), 10453–10460 (2015). https://doi.org/10.1021/acsnano.5b04680

206. Z. Chen, Y. Hu, H. Zhuo, L. Liu, S. Jing, L. Zhong, X. Peng, R.-C. Sun, Compressible, elastic, and pressure-sensitive carbon aerogels derived from 2D Titanium carbide nanosheets and bacterial cellulose for wearable sensors. Chem. Mater. **31**(9), 3301–3312 (2019). https://doi.org/10.1021/acs.chemmater.9b00259

207. X. Zang, X. Wang, J. Xia, Y. Chai, X. Ma et al., Ab Initio design of graphene block enables ultrasensitivity, multimeter-like range switchable pressure sensor. Adv. Mater. Technol. **4**(3), 1800531 (2019). https://doi.org/10.1002/admt.201800531

208. T. Yang, H. Xiang, C. Qin, Y. Liu, X. Zhao et al., Highly sensitive 1T-MoS_2 pressure sensor with wide linearity based on hierarchical microstructures of leaf vein as spacer. Adv. Electron. Mater. **6**(1), 1900916 (2020). https://doi.org/10.1002/aelm.201900916

209. W. Qiugu, H. Wei, D. Liang, Graphene "microdrums" on a freestanding perforated thin membrane for high sensitivity MEMS pressure sensors. Nanoscale **8**(14), 7663–7671 (2016). https://doi.org/10.1039/c5nr09274d

210. S.-E. Zhu, M.K. Ghatkesar, C. Zhang, G.C.A.M. Janssen, Graphene based piezoresistive pressure sensor. Appl. Phys. Lett. **102**(16), 161904 (2013). https://doi.org/10.1063/1.4802799

211. J. Zheng, X. Tang, Z. Yang, Z. Liang, Y. Chen et al., Few-layer phosphorene-decorated microfiber for all-optical thresholding and optical modulation. Adv. Opt. Mater. **5**(9), 1700026 (2017). https://doi.org/10.1002/adom.201700026

212. J. Zheng, Z. Yang, C. Si, Z. Liang, X. Chen et al., Black phosphorus based all-optical-signal-processing: toward high performances and enhanced stability. ACS Photonics **4**(6), 1466–1476 (2017). https://doi.org/10.1021/acsphotonics.7b00231

213. C. Wang, Y. Wang, X. Jiang, J. Xu, W. Huang et al., MXene Ti3C2Tx: a promising photothermal conversion material and application in all-optical modulation and all-optical information loading. Adv. Opt. Mater. **7**(8), 1900060 (2019). https://doi.org/10.1002/adom.201900060

214. Y. Wang, W. Huang, J. Zhao, H. Huang, C. Wang et al., A bismuthene-based multifunctional all-optical phase and intensity modulator enabled by photothermal effect. J. Mater. Chem. C **7**(4), 871–878 (2019). https://doi.org/10.1039/c8tc05513k

215. L. Wu, W. Huang, Y. Wang, J. Zhao, D. Ma et al., 2D tellurium based high-performance all-optical nonlinear photonic

devices. Adv. Funct. Mater. **29**(4), 1806346 (2019). https://doi.org/10.1002/adfm.201806346

216. S. Chen, L. Miao, X. Chen, Y. Chen, C. Zhao et al., Few-layer topological insulator for all-optical signal processing using the nonlinear Kerr effect. Adv. Opt. Mater. **3**(12), 1769–1778 (2015). https://doi.org/10.1002/adom.201500347

217. Y. Song, Y. Chen, X. Jiang, Y. Ge, Y. Wang et al., Nonlinear few-layer MXene-assisted all-optical wavelength conversion at telecommunication band. Adv. Opt. Mater. **7**(18), 1801777 (2019). https://doi.org/10.1002/adom.201801777

218. Y. Wang, F. Zhang, X. Tang, X. Chen, Y. Chen et al., All-optical phosphorene phase modulator with enhanced stability under ambient conditions. Laser Photonics Rev. **12**(6), 1800016 (2018). https://doi.org/10.1002/lpor.201800016

219. L. Wu, K. Chen, W. Huang, Z. Lin, J. Zhao et al., Perovskite $CsPbX_3$: a promising nonlinear optical material and its applications for ambient all-optical switching with enhanced stability. Adv. Opt. Mater. **6**(19), 1800400 (2018). https://doi.org/10.1002/adom.201800400

220. L. Wu, Y. Dong, J. Zhao, D. Ma, W. Huang et al., Kerr nonlinearity in 2D graphdiyne for passive photonic diodes. Adv. Mater. **31**(14), e1807981 (2019). https://doi.org/10.1002/adma.201807981

221. L. Wu, X. Jiang, J. Zhao, W. Liang, Z. Li et al., MXene-based nonlinear optical information converter for all-optical modulator and switcher. Laser Photonics Rev. **12**(12), 1800215 (2018). https://doi.org/10.1002/lpor.201800215

222. L. Wu, Z. Xie, L. Lu, J. Zhao, Y. Wang et al., Few-layer tin sulfide: a promising black-phosphorus-analogue 2D material with exceptionally large nonlinear optical response, high stability, and applications in all-optical switching and wavelength conversion. Adv. Opt. Mater. **6**(2), 1700985 (2018). https://doi.org/10.1002/adom.201700985

223. Q. Wu, S. Chen, Y. Wang, L. Wu, X. Jiang et al., MZI-based all-optical modulator using MXene $Ti_3C_2T_x$ (T = F, O, or OH) deposited microfiber. Adv. Mater. Technol. **4**(4), 1800532 (2019). https://doi.org/10.1002/admt.201800532

224. Y. Wang, W. Huang, C. Wang, J. Guo, F. Zhang et al., An all-optical, actively Q-switched fiber laser by an anti-monene-based optical modulator. Laser Photonics Rev. **13**(3), 1800313 (2019). https://doi.org/10.1002/lpor.201800313

225. H. Moon, J. Bang, S. Hong, G. Kim, J.W. Roh, J. Kim, W. Lee, Strong thermopower enhancement and tunable power factor via semimetal to semiconductor transition in a transition-metal dichalcogenide. ACS Nano **13**(11), 13317–13324 (2019). https://doi.org/10.1021/acsnano.9b06523

226. H. Usui, K. Kuroki, S. Nakano, K. Kudo, M. Nohara, Pudding-mold-type band as an origin of the large seebeck coefficient coexisting with metallic conductivity in carrier-doped $FeAs_2$ and $PtSe_2$. J. Electron. Mater. **43**(6), 1656–1661 (2014). https://doi.org/10.1007/s11664-013-2823-5

227. R. Peng, Y. Ma, B. Huang, Y. Dai, Two-dimensional Janus PtSSe for photocatalytic water splitting under the visible or infrared light. J. Mater. Chem. A **7**(2), 603–610 (2019). https://doi.org/10.1039/c8ta09177c

228. S.-D. Guo, X.-S. Guo, Y. Deng, Tuning the electronic structures and transport coefficients of Janus PtSSe monolayer with biaxial strain. J. Appl. Phys. **126**(15), 154301 (2019). https://doi.org/10.1063/1.5124677

229. W.-L. Tao, J.-Q. Lan, C.-E. Hu, Y. Cheng, J. Zhu, H.-Y. Geng, Thermoelectric properties of Janus MXY (M = Pd, Pt; X, Y = S, Se, Te) transition-metal dichalcogenide monolayers from first principles. J. Appl. Phys. **127**(3), 035101 (2020). https://doi.org/10.1063/1.5130741